



HAL
open science

Finite Difference Time Domain Method For Grating Structures

F.I. Baida, A. Belkhir

► **To cite this version:**

F.I. Baida, A. Belkhir. Finite Difference Time Domain Method For Grating Structures. E. Popov. Gratings: Theory and Numeric Applications, AMU (PUP), pp.9.1-9.36, 2012, 978-2-8539-9860-4. hal-00782306

HAL Id: hal-00782306

<https://hal.science/hal-00782306>

Submitted on 29 Jan 2013

HAL is a multi-disciplinary open access archive for the deposit and dissemination of scientific research documents, whether they are published or not. The documents may come from teaching and research institutions in France or abroad, or from public or private research centers.

L'archive ouverte pluridisciplinaire **HAL**, est destinée au dépôt et à la diffusion de documents scientifiques de niveau recherche, publiés ou non, émanant des établissements d'enseignement et de recherche français ou étrangers, des laboratoires publics ou privés.

GRATINGS: THEORY AND NUMERIC APPLICATIONS

Tryfon Antonakakis
Fadi Baïda
Abderrahmane Belkhir
Kirill Cherednichenko
Shane Cooper
Richard Craster
Guillaume Demesy
John DeSanto
G rard Granet

Boris Gralak
S bastien Guenneau
Daniel Maystre
Andr  Nicolet
Brian Stout
Fr d ric Zolla
Benjamin Vial

Evgeny Popov, Editor

Institut Fresnel, Universit  d'Aix-Marseille, Marseille, France
Femto, Universit  de Franche-Compt , Besan on, France
Institut Pascal, Universit  Blaise Pascal, Clermont-Ferrand, France
Colorado School of Mines, Golden, USA
CERN, Geneva, Switzerland
Imperial College London, UK
Cardiff University, Cardiff, UK
Universit  Mouloud Mammeri, Tizi-Ouzou, Algeria

ISBN: 2-85399-860-4

www.fresnel.fr/numerical-grating-book

ISBN: 2-85399-860-4

First Edition, 2012

World Wide Web:

www.fresnel.fr/numerical-grating-book

Institut Fresnel, Université d'Aix-Marseille, CNRS
Faculté Saint Jérôme,
13397 Marseille Cedex 20,
France

Gratings: Theory and Numeric Applications, Evgeny Popov, editor (Institut Fresnel, CNRS, AMU, 2012)

Copyright © 2012 by Institut Fresnel, CNRS, Université d'Aix-Marseille, All Rights Reserved

Chapter 9:

Finite Difference Time Domain Method for Grating Structures

Fadi Issam Baida

and

Abderrahmane Belkhir

Table of Contents:

9.1	Fundamentals of the FDTD method	1
9.1.1	The Yee's algorithm	1
9.1.2	Spatiotemporal criteria of convergence	6
9.1.3	Absorbing boundary conditions - Perfectly Matched Layers	7
9.1.4	Dispersive media	8
9.1.4.1	Drude Model	9
9.1.4.2	Drude-Lorentz Model	10
9.1.4.3	Drude critical points model	11
9.2	Band gap calculation for 2D periodic structures	13
9.2.1	In-plane propagation: <i>TE</i> and <i>TM</i> polarizations	13
9.2.2	Off-plane propagation	14
9.2.3	Periodic boundary conditions	14
9.2.4	Some examples of band gap calculation	16
9.3	Scattering calculation for 3D biperiodic nanostructures	20
9.3.1	Position of the problem: New $\vec{P} - \vec{Q}$ variables	21
9.3.2	Split Field Method	23
9.3.3	Absorbing boundary conditions : PML	25
9.3.4	SFM-FDTD in dispersive media	25
9.3.5	3D-SFM-FDTD application: EOT at oblique incidence through AAA structures	28
9.4	Conclusion	32

Chapter 9

Finite Difference Time Domain Method For Grating Structures

Fadi Issam Baida¹ and Abderrahmane Belkhir²

¹ *Institut FEMTO-ST, Département d'Optique P.M. Duffieux, UMR 6174 CNRS
Université de Franche-Comté, 25030 Besançon Cedex, France*

² *Université Mouloud Mammeri, Laboratoire de Physique et Chimie Quantique,
Tizi-Ouzou, Algeria
fbaida@univ-fcomte.fr*

The Finite Difference Time Domain method (FDTD), based on the Yee's scheme, is one of the most commonly used time methods for the modeling of electromagnetic waves propagation and diffraction. It was first introduced by Yee in 1966 [1] in the context of differential equations resolution and the first articles recommending its futur applications are published from 1975 [2, 3, 4]. Due to the simplicity of its implementation and the rapid growth of computing capacity, the FDTD is gaining users in all areas of electromagnetism applications. It allows a real-time monitoring of the electromagnetic wave evolution in any kind of environment (dielectric, metal, plasma...). Its theoretical formulation is very easy since it requires no matrix inversion and could take into account the more complex geometric shapes of objects in the studied system. In addition, using this time domain method, a wide spectral range characterization can be obtained from one temporal calculation via a simple Fourier transform.

In this chapter, we present a brief review on the fundamentals of the FDTD method. We show how to adapt it to the calculation of the photonic band gap structures in the case of 2D periodic (invariant in the third direction) structures. The both in-plane, for the TE and TM polarizations, and off-plane propagations are considered. The last part of this chapter is devoted to FDTD general formulation, based on the Split Field Method technique, for the modeling of bi-periodic gratings that are finished according to the third direction.

9.1 Fundamentals of the FDTD method

9.1.1 The Yee's algorithm

The FDTD method is based on the numerical resolution of the Maxwell's equations using a centered finite difference schema to approximate the partial derivatives both in time and space.

Let us start from these equations expressed in their differential formulation:

$$\nabla \times \vec{E} = -\frac{\partial \vec{B}}{\partial t} \quad (9.1)$$

$$\nabla \times \vec{H} = \frac{\partial \vec{D}}{\partial t} \quad (9.2)$$

The electromagnetic properties of the medium are described through the so-called constitutive relationships:

$$\vec{D} = \varepsilon \vec{E} \quad (9.3)$$

$$\vec{B} = \mu \vec{H} \quad (9.4)$$

ε and μ are respectively the dielectric permittivity and magnetic permeability of the medium.

In a Cartesian coordinate system (O, x, y, z) , the Maxwell's equations in the time domain are written as:

$$\frac{\partial H_x}{\partial t} = \frac{1}{\mu} \left[\frac{\partial E_y}{\partial z} - \frac{\partial E_z}{\partial y} \right] \quad (9.5.a)$$

$$\frac{\partial H_y}{\partial t} = \frac{1}{\mu} \left[\frac{\partial E_z}{\partial x} - \frac{\partial E_x}{\partial z} \right] \quad (9.5.b)$$

$$\frac{\partial H_z}{\partial t} = \frac{1}{\mu} \left[\frac{\partial E_x}{\partial y} - \frac{\partial E_y}{\partial x} \right] \quad (9.5.c)$$

$$\frac{\partial E_x}{\partial t} = \frac{1}{\varepsilon} \left[\frac{\partial H_z}{\partial y} - \frac{\partial H_y}{\partial z} \right] \quad (9.5.d)$$

$$\frac{\partial E_y}{\partial t} = \frac{1}{\varepsilon} \left[\frac{\partial H_x}{\partial z} - \frac{\partial H_z}{\partial x} \right] \quad (9.5.e)$$

$$\frac{\partial E_z}{\partial t} = \frac{1}{\varepsilon} \left[\frac{\partial H_y}{\partial x} - \frac{\partial H_x}{\partial y} \right] \quad (9.5.f)$$

The numerical treatment of the partial differential equations 9.5 requires a space and time discretization. The calculation volume, shown in figure 9.1 is a rectangular parallelepiped divided into $(N_x \times N_y \times N_z)$ cells, each one with elementary volume $(\Delta x \times \Delta y \times \Delta z)$ where Δx , Δy and Δz are the spatial discretization steps according to the Ox , Oy and Oz directions respectively.

Each well defined node of the grid is associated with a triplet of integers (i, j, k) so that the coordinates (x_i, y_j, z_k) of the node satisfy:

$$x_i = i \cdot \Delta x$$

$$y_j = j \cdot \Delta y$$

$$z_k = k \cdot \Delta z$$

The computational time is also discretized with a Δt time step. Each computing time t is associated with the integer n defining the number of temporal sampling:

$$t = n \cdot \Delta t$$

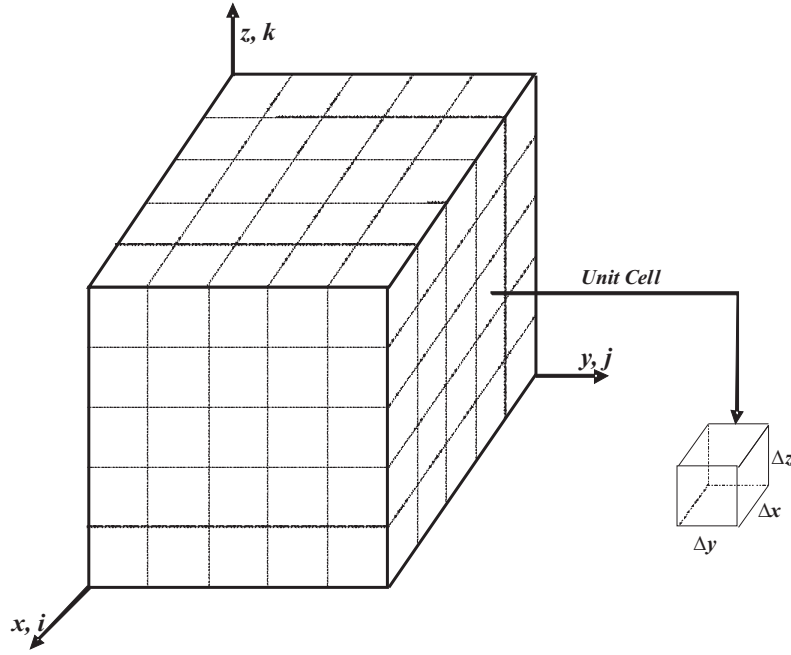


Figure 9.1: An exemple of the FDTD calculation volume.

Temporal and spatial derivatives of the field components ($E_x, E_y, E_z, H_x, H_y, H_z$) are approximated from their Taylor development to the first order. Thus, if U is one of these components, we will adopt the following notation:

$$U(x_i, y_j, z_k, t) = U_{i,j,k}^n \quad (9.6)$$

The temporal derivative of the U component at t time and (x_i, y_j, z_k) node is approximated with finite centred difference as follows:

$$\left[\frac{\partial U}{\partial t} \right]_{i,j,k} = \frac{U_{i,j,k}^{n+\frac{1}{2}} - U_{i,j,k}^{n-\frac{1}{2}}}{\Delta t} + 0([\Delta t]^2) \quad (9.7)$$

The spatial derivatives of the U component are approximated in the same manner:

$$\left[\frac{\partial U}{\partial x} \right]_{j,k,n} = \frac{U_{i+\frac{1}{2},j,k}^n - U_{i-\frac{1}{2},j,k}^n}{\Delta x} + 0([\Delta x]^2) \quad (9.8.a)$$

$$\left[\frac{\partial U}{\partial y} \right]_{i,k,n} = \frac{U_{i,j+\frac{1}{2},k}^n - U_{i,j-\frac{1}{2},k}^n}{\Delta y} + 0([\Delta y]^2) \quad (9.8.b)$$

$$\left[\frac{\partial U}{\partial z} \right]_{i,j,n} = \frac{U_{i,j,k+\frac{1}{2}}^n - U_{i,j,k-\frac{1}{2}}^n}{\Delta z} + 0([\Delta z]^2) \quad (9.8.c)$$

As explicitly mentioned in equations 9.8, the use of centered difference scheme allows a precision of the second order even if a first order Taylor development is considered. This greatly enhances the numerical convergence of the FDTD algorithm.

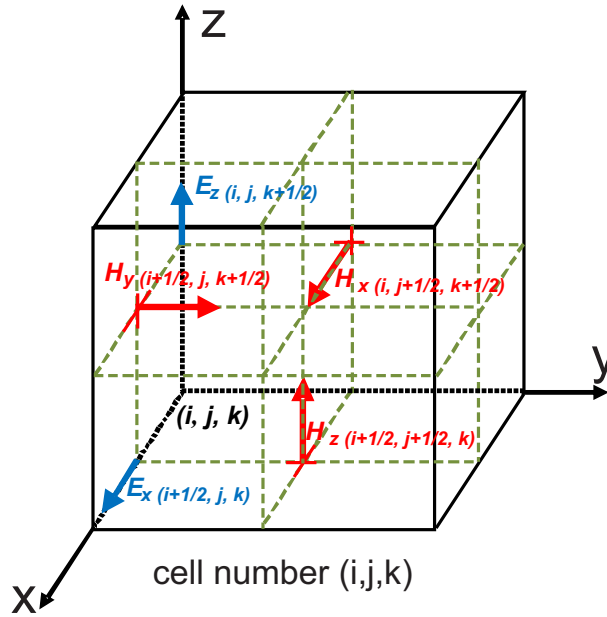


Figure 9.2: Spatial discretization : Yee's cell.

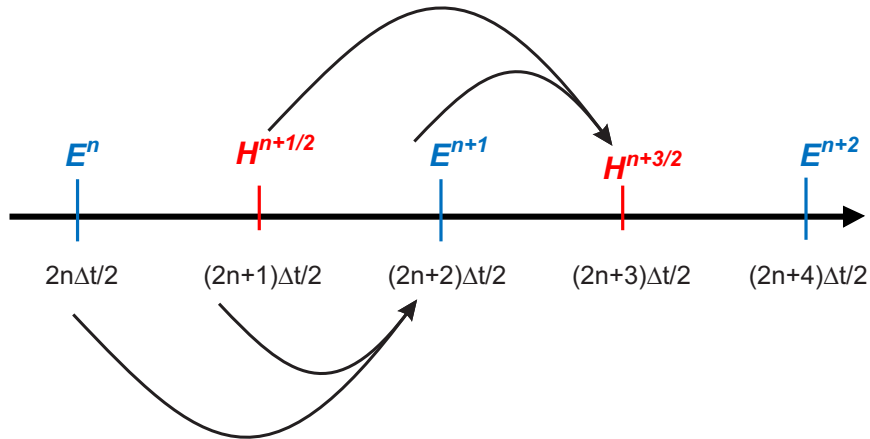


Figure 9.3: Temporal discretization into the Yee's scheme.

Yee's algorithm

The algorithm proposed by Kane Yee in 1966 [1] uses in a clever way this discretization for solving the system of equations (9.5). In the Yee's scheme, the electromagnetic field components are located at different points in a unit cell (Figure9.2). The electric field components are calculated along the edges of the cell while the perpendicular magnetic field components are calculated at the centers of the cell faces. Thus, each electric field component is surrounded by four magnetic field components and similarly for each magnetic field component.

The temporal increment into the Yee's scheme is done through a "leapfrog" discretization schema. The field components \vec{H} (or \vec{E}) are calculated at times odd multiples of the half time step $\frac{\Delta t}{2}$, while the field components \vec{E} (respectively \vec{H}) are updated at the times even multiples of $\frac{\Delta t}{2}$ as shown in figure 9.3. Such a discretization allows evaluating the time derivatives by keeping a centered difference schema as for spatial derivatives.

Consequently, replacing the partial derivatives in equations (9.5) by central difference (9.7-9.8), according to the Yee's scheme leads to the updated equations of electromagnetic components in the FDTD algorithm:

$$H_x^{n+\frac{1}{2}}(i, j+\frac{1}{2}, k+\frac{1}{2}) = H_x^{n-\frac{1}{2}}(i, j+\frac{1}{2}, k+\frac{1}{2}) - \frac{\Delta t}{\mu_0 \Delta} \left\{ \left[E_z^n(i, j+1, k+\frac{1}{2}) - E_z^n(i, j, k+\frac{1}{2}) \right] + \left[E_y^n(i, j+\frac{1}{2}, k) - E_y^n(i, j+\frac{1}{2}, k+1) \right] \right\} \quad (9.9.a)$$

$$H_y^{n+\frac{1}{2}}(i+\frac{1}{2}, j, k+\frac{1}{2}) = H_y^{n-\frac{1}{2}}(i+\frac{1}{2}, j, k+\frac{1}{2}) - \frac{\Delta t}{\mu_0 \Delta} \left\{ \left[E_x^n(i+\frac{1}{2}, j, k+1) - E_x^n(i+\frac{1}{2}, j, k) \right] + \left[E_z^n(i, j, k+\frac{1}{2}) - E_z^n(i+1, j, k+\frac{1}{2}) \right] \right\} \quad (9.9.b)$$

$$H_z^{n+\frac{1}{2}}(i+\frac{1}{2}, j+\frac{1}{2}, k) = H_z^{n-\frac{1}{2}}(i+\frac{1}{2}, j+\frac{1}{2}, k) - \frac{\Delta t}{\mu_0 \Delta} \left\{ \left[E_y^n(i+1, j+\frac{1}{2}, k) - E_y^n(i, j+\frac{1}{2}, k) \right] + \left[E_x^n(i+\frac{1}{2}, j, k) - E_x^n(i+\frac{1}{2}, j+1, k) \right] \right\} \quad (9.9.c)$$

$$E_x^{n+1}(i+\frac{1}{2}, j, k) = E_x^n(i+\frac{1}{2}, j, k) + \frac{\Delta t}{\epsilon \Delta} \left\{ \left[H_z^n(i+\frac{1}{2}, j+\frac{1}{2}, k) - H_z^n(i+\frac{1}{2}, j-\frac{1}{2}, k) \right] + \left[H_y^n(i+\frac{1}{2}, j, k-\frac{1}{2}) - H_y^n(i+\frac{1}{2}, j, k+\frac{1}{2}) \right] \right\} \quad (9.9.d)$$

$$E_y^{n+1}(i, j+\frac{1}{2}, k) = E_y^n(i, j+\frac{1}{2}, k) + \frac{\Delta t}{\epsilon \Delta} \left\{ \left[H_x^n(i, j+\frac{1}{2}, k+\frac{1}{2}) - H_x^n(i, j+\frac{1}{2}, k-\frac{1}{2}) \right] + \left[H_z^n(i-\frac{1}{2}, j+\frac{1}{2}, k) - H_z^n(i+\frac{1}{2}, j+\frac{1}{2}, k) \right] \right\} \quad (9.9.e)$$

$$E_z^{n+1}(i, j, k+\frac{1}{2}) = E_z^n(i, j, k+\frac{1}{2}) + \frac{\Delta t}{\epsilon \Delta} \left\{ \left[H_y^n(i+\frac{1}{2}, j, k+\frac{1}{2}) - H_y^n(i-\frac{1}{2}, j, k+\frac{1}{2}) \right] + \left[H_x^n(i, j-\frac{1}{2}, k+\frac{1}{2}) - H_x^n(i, j+\frac{1}{2}, k+\frac{1}{2}) \right] \right\} \quad (9.9.f)$$

Let us note that this last equation system can be simplified significantly in case of 2D structures (see section 2 of this chapter).

For the modeling of structures with a symmetry of revolution, a basis change from Cartesian to cylindrical coordinates is strongly recommended to accurately describe the fine details of the samples and to make more flexible the FDTD calculation codes. In these so-called BOR-FDTD (Body of Revolution FDTD) codes, the symmetry of revolution is exploited to express

the azimuthal dependence (ϕ) of the electromagnetic fields as Fourier series. BOR-FDTD algorithm can, in this case, compute solutions for all Fourier modes through one simulation per mode. This code is commonly called 2.5D since the azimuthal field variation is analytically accounted for. Thus, there is no gridding in the ϕ -direction. This implies that the BOR-FDTD algorithm is two-dimensional in terms of computer resource usage even 3D structures are modeled.

9.1.2 Spatiotemporal criteria of convergence

As all explicit schemes, Yee's algorithm is subjected to a stability condition setting the time step from the space discretization. Arbitrary values of spatiotemporal discretization can lead to infinite solutions of the electromagnetic field. Stability problems in explicit numerical methods have been analyzed in detail by Courant, Friedrichs and Levy [5] and Von Neumann, from a mathematically rigorous approach. This analysis shows that the explicit schemes are stable under a condition called CFL (for Current, Friedrich and Levy) and applied to the FDTD method in the case of a regular mesh [6]:

$$\Delta t \leq \left[v_{max} \cdot \sqrt{\frac{1}{\Delta x^2} + \frac{1}{\Delta y^2} + \frac{1}{\Delta z^2}} \right]^{-1} \quad (9.10)$$

where v_{max} is the maximum velocity of light propagation in the studied system, generally the velocity of light in vacuum.

In case of uniforme mesh ($\Delta x = \Delta y = \Delta z = \Delta$), the CFL criterion becomes:

$$\Delta t \leq \frac{1}{v_{max}} \cdot \frac{\Delta}{\sqrt{3}} \quad \text{in } 3D \quad (9.11)$$

$$\Delta t \leq \frac{1}{v_{max}} \cdot \frac{\Delta}{\sqrt{2}} \quad \text{in } 2D \quad (9.12)$$

However, it is possible to overcome the restrictive assumption of regular mesh that achieves the above result with the following generalized criterion:

$$\Delta t \leq \left[v_{max} \cdot \sqrt{\frac{1}{\Delta x_{min}^2} + \frac{1}{\Delta y_{min}^2} + \frac{1}{\Delta z_{min}^2}} \right]^{-1} \quad (9.13)$$

where Δx_{min} , Δy_{min} et Δz_{min} are the smallest step in the three directions x , y and z respectively.

In addition to the numerical instability problem, the transition from continuous forms of Maxwell's equations to the discrete numerical approximations can cause a parasitic effect called "numerical dispersion". This is due to the fact that numerical signals are propagated over time in the FDTD grid, with a phase velocity less than the actual velocity. This dispersion varies with frequency, propagation direction in the grid and the spatial discretization [6]. Numerical dispersion errors increase with the signal frequency and size of the computational domain, thus

making the simulation results less reliable. They may appear in various forms: phase error, signal distortion, loss of amplitude, pulse broadening ...

The solution to this problem requires a very fine mesh in the FDTD grid, so that the maximum discretization is of the order $\lambda_{min}/20$ [6], λ_{min} being the minimum wavelength of propagating waves in the FDTD grid.

9.1.3 Absorbing boundary conditions - Perfectly Matched Layers

Such conditions allow us to describe open systems where emitted or reflected waves propagate to infinity. Indeed, the limited memory space of computers requires users to truncate their FDTD computational domain. At the limits of this truncated domain, components of the electromagnetic field can not be calculated by the discretized equations (9.9). Therefore special treatment at the borders is needed to avoid the incident electromagnetic wave on these "edges" does reflect back and contaminate the actual physical signal. One of the most widely used technique is that proposed by Berenger [7] called Perfectly Matched Layer (PML). This technique consists of adding around the studied domain not necessarily physical layer causing no reflection and almost totally absorbing all the propagating electromagnetic field. Its use is based on the condition of impedance matching of two waves at the interface between two media with the same index but which one is absorbing (with nonzero electrical conductivity σ and magnetic equivalent conductivity σ^* as shown in figure 9.4).

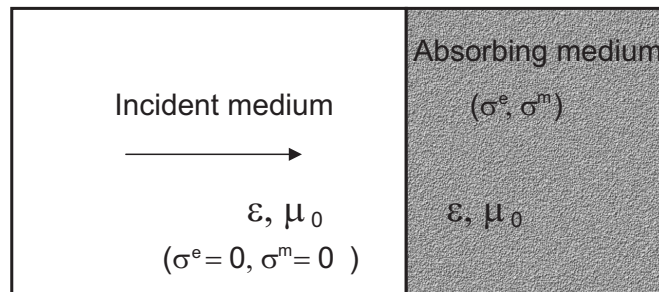


Figure 9.4: Impedance matching principle.

This condition is expressed as:

$$\frac{\sigma}{\varepsilon} = \frac{\sigma^*}{\mu_0} \quad (9.14)$$

Thus, a magnetic conductivity is needed to fulfill this impedance matching condition. In addition, absorption is needed only for components of the fields that propagates perpendicularly to the interface (the FDTD window border) and not in the parallel direction. Bérenger solved this problem by proposing an artificially biaxial absorbing medium. The absorption is not zero in the direction normal to the interface between the two media and is zero along the axis parallel to the interface. In the PML medium, the incident plane wave is split into two fictitious waves (see figure 9.5):

1) A wave propagating at normal incidence and satisfying the equation 9.14. This wave is attenuated and absorbed by the PML medium and undergoes only very low reflectivity to the incident medium.

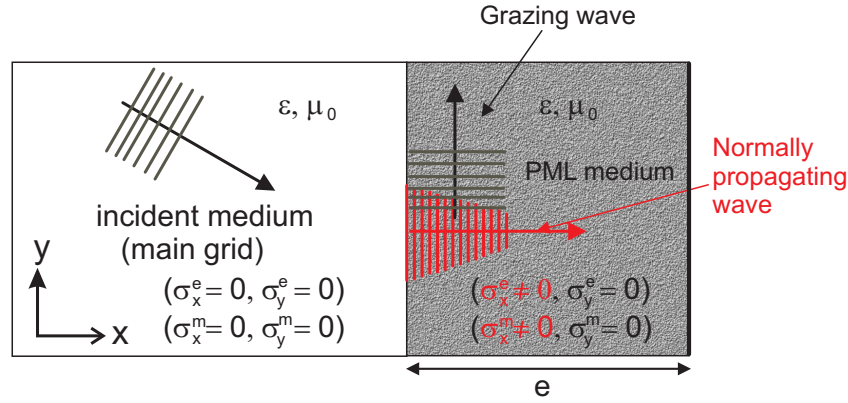


Figure 9.5: Schematic of the PML principle.

2) A second grazing incidence wave that shows no absorption in the PML medium. This wave, propagating parallel to the interface between two media undergoes no reflection and sees a medium identical to that of the main grid window.

Abrupt changes in conductivities at this interface degrade the performances of absorption. This effect is, however, reduced by imposing a progressive variation of the absorption according to a polynomial law given by [7]:

$$\sigma = \sigma_{max} \left(\frac{x_{pml}}{e} \right)^m \quad (9.15)$$

where σ_{max} is the maximum value of the conductivity, x_{pml} represents the depth in the PML region measured from the interface, e denotes the thickness of the PML layer and m is the polynomial order generally fixed to 2.

Let us note that in the case of gratings such conditions are not necessary according to the periodicity directions. The absorbing boundaries conditions are hereby replaced by Floquet-Bloch periodic conditions in order to describe periodic structures (see section 2 of this chapter). Nevertheless, for a 2D periodic structure, PML are needed in the third direction where the structure is usually finite.

9.1.4 Dispersive media

The dispersive media, such as metals in the optical range, are characterized by a complex permittivity frequency dependent $\epsilon(\omega) = \epsilon'(\omega) + i\epsilon''(\omega)$. As the FDTD method is temporal, in such environments the direct implementation of the above equations, in which appear explicitly permittivity and hence the frequency, is impossible. The solution for this problem is to calculate the displacement vector \vec{D} components in the classical Yee's scheme and then back to electrical field components using the constitutive equation of the medium established in the frequency domain $\vec{D}(\omega) = \epsilon(\omega)\vec{E}(\omega)$. The temporal nature of the FDTD needs a temporal constitutive equation written as a convolution product $\vec{D}(t) = \epsilon(t) \otimes \vec{E}(t)$. It is a non local relationship whose resolution requires the knowledge of the electric field at all previous times. Numerically, this leads to a storage of a very large amount of data and therefore requires to have a very large memory space. This issue can be bypassed using analytical models describing the dielectric function $\epsilon(\omega)$ of these metals. The choice of adapted analytical model depends on the type of metal as well as the spectral range of study.

9.1.4.1 Drude Model

The Drude model of free electrons [8, 9] for the dielectric function which, although based on a purely classical approach, can well account for intraband transitions. In this model, firstly proposed in 1908 by P. Drude, a gas of free electrons moving in a immobile metal ions lattice. Thus, the electron-electron interactions and electron-ions are not taken into account and the movement of all the electron cloud is thus the average of the movements of individual electrons. The relative permittivity given by this model is:

$$\epsilon_D = \epsilon_\infty - \frac{\omega_D^2}{\omega^2 + i\omega\gamma_D} \quad (9.16)$$

where ω_D is the "plasma frequency" of the metal and ϵ_∞ its relative permittivity at infinite frequencies. γ_D represents a damping term that is inversely proportional to the relaxation time.

FDTD implementation of the Drude model

The principle consists in replacing the electric field vector \vec{E} by \vec{D}/ϵ in Maxwell's equations in order to eliminate ϵ term. In dispersive media, equations (9.9.d, 9.9.e et 9.9.f) are replaced by:

$$D_x^{n+1}(i+\frac{1}{2},j,k) = D_x^n(i+\frac{1}{2},j,k) + \frac{\Delta t}{\Delta} \left\{ \left[H_z^n(i+\frac{1}{2},j+\frac{1}{2},k) - H_z^n(i+\frac{1}{2},j-\frac{1}{2},k) \right] + \left[H_y^n(i+\frac{1}{2},j,k-\frac{1}{2}) - H_y^n(i+\frac{1}{2},j,k+\frac{1}{2}) \right] \right\} \quad (9.17)$$

$$D_y^{n+1}(i,j+\frac{1}{2},k) = E_y^n(i,j+\frac{1}{2},k) + \frac{\Delta t}{\Delta} \left\{ \left[H_x^n(i,j+\frac{1}{2},k+\frac{1}{2}) - H_x^n(i,j+\frac{1}{2},k-\frac{1}{2}) \right] + \left[H_z^n(i-\frac{1}{2},j+\frac{1}{2},k) - H_z^n(i+\frac{1}{2},j+\frac{1}{2},k) \right] \right\} \quad (9.18)$$

$$D_z^{n+1}(i,j,k+\frac{1}{2}) = D_z^n(i,j,k+\frac{1}{2}) + \frac{\Delta t}{\Delta} \left\{ \left[H_y^n(i+\frac{1}{2},j,k+\frac{1}{2}) - H_y^n(i-\frac{1}{2},j,k+\frac{1}{2}) \right] + \left[H_x^n(i,j-\frac{1}{2},k+\frac{1}{2}) - H_x^n(i,j+\frac{1}{2},k+\frac{1}{2}) \right] \right\} \quad (9.19)$$

Once the components of the displacement vector \vec{D} are updated from the previous equations, we proceed to the determination of the \vec{E} components using the relation $\vec{D} = \epsilon(\omega)\vec{E}$. Replacing $\epsilon(\omega)$ by its expression given by the Drude model, we get to:

$$(\omega^2 + i\omega\gamma_D)\vec{D} = \epsilon_0\epsilon_\infty(\omega^2 + i\omega\gamma_D)\vec{E} - \epsilon_0\omega_D^2\vec{E} \quad (9.20)$$

Assuming time dependence of electromagnetic field in $e^{-i\omega t}$, a simple Fourier transform ($\omega \rightarrow t$) of this last equation leads to:

$$\frac{d^2 \vec{D}}{dt^2} + \gamma_D \frac{d \vec{D}}{dt} = \epsilon_0 \left(\epsilon_\infty \frac{d^2 \vec{E}}{dt^2} + \epsilon_\infty \gamma_D \frac{d \vec{E}}{dt} + \omega_D^2 \vec{E} \right)$$

The partial derivatives of this equations are then replaced by their expressions through the centered finite difference schema. The electric field updated equation in the dispersive media is then obtained:

$$\xi \vec{E}^{n+1} = -\chi \vec{E}^{n-1} + 4\epsilon_\infty \epsilon_0 \vec{E}^n + \vec{D}^{n+1} [\gamma_D \Delta t + 2] - 4\vec{D}^n + [-\gamma_D \Delta t + 2] \vec{D}^{n-1} \quad (9.21)$$

with $\xi = \epsilon_0 [\omega_D^2 \Delta t^2 + \epsilon_\infty \gamma_D \Delta t + 2\epsilon_\infty]$ and $\chi = \epsilon_0 [\omega_D^2 \Delta t^2 - \gamma_D \epsilon_\infty \Delta t + 2\epsilon_\infty]$. Due to the dispersion, an additional step of calculation is necessary. It consists of determining the displacement field components for all nodes representing the dispersive media. In addition and as can be seen in equation (9.21), we need to store the \vec{E} and \vec{D} components on two time steps, which has the effect of increasing the memory space to be allocated and the computation time.

9.1.4.2 Drude-Lorentz Model

In addition to the conduction electrons, the Drude-Lorentz model takes into account the bound electrons. The interband transition of electrons from filled bands to the conduction band can significantly influence the optical response. In alkali metals, these transitions occur at high frequencies and provide only small corrections to the dielectric function in the optical domain. These metals are well described by the Drude model. On the other side, in noble metals a correction must be made to the dielectric function. It is due to transitions between the bands d and the conduction band s-p. The contribution of bound electrons to the dielectric function can be described by the Lorentz model. To the above Drude dielectric function, a Lorentzian term is added:

$$\epsilon_{DL}(\omega) = \epsilon_D(\omega) + \epsilon_L(\omega)$$

Estimating $\epsilon_L(\omega)$, the bound electrons are described by forced and damped harmonic oscillators. Vial *et al.* [10] suggested a single oscillator leading to a single Lorentzian additional term to well describe the permittivity of gold in the optical range compared with the classical Drude model. In this case, the relative dielectric function is:

$$\epsilon_{DL}(\omega) = \epsilon_\infty - \frac{\omega_p^2}{\omega^2 + i\omega\gamma} - \frac{\Delta\epsilon \cdot \Omega_L^2}{(\omega^2 - \Omega_L^2) + i\Gamma_L\omega} \quad (9.22)$$

where Γ_L et Ω_L stand for the spectral width and the strength of the Lorentz oscillator respectively. $\Delta\epsilon$ is a weighting factor.

The FDTD implementation of this model can be done with the Auxilliary Differential Equations (ADE) method previously described above in the case of the Drude model or the so-called Recursive Convolution (RC) method [10]. Because of the additional Lorentzian term, its use requires the introduction of additional intermediate electromagnetic components in the algorithm. Thus, a larger memory space is required compared to the case of the Drude model. In general, many involving multiple oscillators Lorentz terms are needed to accurately model the permittivity of noble metals in the optical range.

9.1.4.3 Drude critical points model

The optical properties of some metals, particularly gold, are more difficult to be analytically described in the visible/near-UV region. This comes from much more important role, in the case of gold, played by interband transitions in this region. Some attempts to add Lorentz oscillators to the classical Drude term to account for these transitions rapidly face limitations [11]. In fact, besides the huge simulation time, increasing the number of parameters (mainly non-physical and not well defined) would not provide more insight than quality fit (itself non-physical) with a polynomial high degree or a simple numerical interpolation of the experimental data.

In order to achieve a reasonable representation of the dielectric function, Etchegoin *et al.* [12] took inspiration from the parametric critical points model developed for semiconductors [13]. This model is very suitable for the description of optical properties of metals (such as gold) for which the band structure is quite complex. In this approach, the frequency dependence of the optical properties of gold in the visible/near-UV may be well described by an analytical formula with three main contributions that can be expressed as follows:

$$\epsilon_{D2CP}(\omega) = \epsilon_{\infty} - \frac{\omega_D^2}{\omega^2 + i\omega\gamma_D} + \sum_{p=1}^{p=2} G_p(\omega) \quad (9.23)$$

with

$$G_p(\omega) = A_p \Omega_p \left(\frac{e^{i\phi_p}}{\Omega_p - \omega - i\Gamma_p} + \frac{e^{-i\phi_p}}{\Omega_p + \omega + i\Gamma_p} \right) \quad (9.24)$$

The two first terms of equation (9.23) represents the standard contribution of the classical Drude Model. The sum in equation (9.23) is the contribution of the inter-band transitions with the amplitude A_p , gap energy Ω_p , phase ϕ_p and broadening Γ_p .

In a comparative study of this Drude critical points (CP) model with the so-called L4 model which consists of four Lorentzian terms [14], Vial *et al.* [15] show the possibility to increase the accuracy of gold and silver permittivity description by using the CP model with fewer parameters to determine and less memory use within the FDTD method.

Implementation of the CP model in FDTD using ADE technique

As in the previous case of the Drude model, the technique is to calculate the displacement vector components by the FDTD equations (9.17,9.18 and 9.19) and determine electrical components using the following relationship:

$$\vec{D} = \epsilon_0 \epsilon_{DCP} \vec{E} \quad (9.25)$$

In the case of the CP model, \vec{D} can be written as the sum of the electric displacement vectors corresponding to each of the contributions in the dielectric function expression:

$$\vec{D} = \vec{D}_D + \sum_{p=1}^2 \vec{D}_{CP} \quad (9.26)$$

with

$$\vec{D}_D = \epsilon_0 \left[\epsilon_\infty - \frac{\omega_p^2}{\omega^2 + i\gamma\omega} \right] \vec{E} \quad (9.27.a)$$

$$\vec{D}_{Cp} = \epsilon_0 A_p \Omega_p \left(\frac{e^{i\phi_p}}{\Omega_p - \omega - i\Gamma_p} + \frac{e^{-i\phi_p}}{\Omega_p + \omega + i\Gamma_p} \right) \vec{E} \quad (9.27.b)$$

As before the temporal evolution of the fields in $e^{-i\omega t}$ is considered. By inverse Fourier transform, we obtain:

$$\left(\frac{\partial^2}{\partial t^2} + \gamma \frac{\partial}{\partial t} \right) \vec{D}_D = \epsilon_0 \epsilon_\infty \left(\frac{\partial^2}{\partial t^2} + \gamma \frac{\partial}{\partial t} + \frac{\omega_p^2}{\epsilon_\infty} \right) \vec{E} \quad (9.28.a)$$

$$\left(\Omega_p^2 + \Gamma_p^2 + \frac{\partial^2}{\partial t^2} + 2\Gamma_p \frac{\partial}{\partial t} \right) \vec{D}_{Cp} = 2\epsilon_0 A_p \Omega_p \left(\sqrt{\Gamma_p^2 + \Omega_p^2} \sin(\theta_p - \phi_p) - \sin \phi_p \frac{\partial}{\partial t} \right) \vec{E} \quad (9.28.b)$$

where: $\theta_p = \arctan\left(\frac{\Omega_p}{\Gamma_p}\right)$

By centered difference discretization of the equation system (9.28) and taking into account the split equation of the displacement vector (9.26), we reach the updated equations system for the electric field vector at each point (i, j, k) of the calculation window:

$$\vec{E}^{n+1} = \frac{1}{\frac{\chi_D}{\alpha_D} + \sum_{p=1}^{p=2} \left(\frac{\chi_p}{\alpha_p} \right)} \left[\vec{D}^{n+1} + \frac{\beta_D}{\alpha_D} \vec{D}_D^{n-1} + \frac{4}{\alpha_D} \vec{D}_D^n - \frac{\delta_D}{\alpha_D} \vec{E}^{n-1} - \frac{4\epsilon_0 \epsilon_\infty}{\alpha_D} \vec{E}^n \right. \\ \left. + \sum_{p=1}^{p=2} \left(\frac{\beta_p}{\alpha_p} \vec{D}_{Cp}^{n-1} - \frac{4}{\alpha_p} \vec{D}_{Cp}^n \right) + \sum_{p=1}^{p=2} \left(\frac{\delta_p}{\alpha_p} \right) \vec{E}^{n-1} \right] \quad (9.29.a)$$

$$\vec{D}_D^{n+1} = \frac{1}{\alpha_D} \left[-\beta_D \vec{D}_D^{n-1} - 4\vec{D}_D^n + \chi_D \vec{E}^{n+1} + \delta_D \vec{E}^{n-1} + 4\epsilon_0 \epsilon_\infty \vec{E}^n \right] \quad (9.29.b)$$

$$\vec{D}_{Cp}^{n+1} = \frac{1}{\alpha_p} \left[-\beta_p \vec{D}_{Cp}^{n-1} + 4\vec{D}_{Cp}^n + \chi_p \vec{E}^{n+1} + \delta_p \vec{E}^{n-1} \right] \quad (9.29.c)$$

with:

$$\alpha_D = -2 - \gamma\Delta t \quad (9.30a)$$

$$\beta_D = -2 + \gamma\Delta t \quad (9.30b)$$

$$\chi_D = \epsilon_0 \epsilon_\infty \left[-2 - \gamma\Delta t - (\omega_p \Delta t)^2 / \epsilon_\infty \right] \quad (9.30c)$$

$$\delta_D = \epsilon_0 \epsilon_\infty \left[-2 + \gamma\Delta t - (\omega_p \Delta t)^2 / \epsilon_\infty \right] \quad (9.30d)$$

$$\alpha_p = [\Omega_p^2 + \Gamma_p^2] \Delta t^2 + 2\Gamma_p \Delta t + 2 \quad (9.30e)$$

$$\beta_p = [\Omega_p^2 + \Gamma_p^2] \Delta t^2 - 2\Gamma_p \Delta t + 2 \quad (9.30f)$$

$$\chi_p = 2A_p \Omega_p \epsilon_0 \left[\Delta t^2 \sqrt{\Omega_p^2 + \Gamma_p^2} \sin(\theta_p - \phi_p) - \Delta t \sin \phi_p \right] \quad (9.30g)$$

$$\delta_p = 2A_p \Omega_p \epsilon_0 \left[\Delta t^2 \sqrt{\Omega_p^2 + \Gamma_p^2} \sin(\theta_p - \phi_p) + \Delta t \sin \phi_p \right] \quad (9.30h)$$

Let us mention that the displacement vector split into three contributions avoids doing appear derivatives of order higher than 2 in the equations system (9.28). As seen on the equations

system (9.29), taking into consideration the two critical points in the FDTD algorithm does not need to store \vec{E} and \vec{D} components over more than two time steps. However, against the Drude model implementation, additional calculation stages appear in order to determine the two parts of the displacement vector corresponding to the two critical contributions.

9.2 Band gap calculation for 2D periodic structures

In this section, we describe how to adapt the FDTD calculation for photonic bandgap structures (PBG) of periodic arrays. The biperiodic structures case is there considered. These 2D structures are photonic crystals (PhC) whose permittivity is periodic in two dimensions (x and y for example) and remains invariant according to the third one (z). They mainly include three main families that are square, triangular and hexagonal lattices. For this type of structures, we can distinguish two kinds of propagation, in the plane (in-plane, $k_z = 0$) and out of plane (off-plane, nonzero k_z). The system of equations (9.5) becomes easier depending on the type of propagation. To illustrate this, let us assume in what follows that the PhC is periodic along the x and y directions and infinite along z direction.

9.2.1 In-plane propagation: TE and TM polarizations

In that case the propagation is done in the plane and the field variation vanishes along the third direction. The system of equations (9.5) is simplified and divided into two independent subsystems giving rise to two polarizations: transverse electric (*TE*) and transverse magnetic (*TM*):

TE Polarization

$$\frac{\partial H_z}{\partial t} = \frac{1}{\mu} \left(\frac{\partial E_x}{\partial y} - \frac{\partial E_y}{\partial x} \right) \quad (9.31a)$$

$$\frac{\partial E_x}{\partial t} = \frac{1}{\varepsilon} \frac{\partial H_z}{\partial y} \quad (9.31b)$$

$$\frac{\partial E_y}{\partial t} = -\frac{1}{\varepsilon} \frac{\partial H_z}{\partial x} \quad (9.31c)$$

TM Polarization

$$\frac{\partial H_x}{\partial t} = -\frac{1}{\mu} \frac{\partial E_z}{\partial y} \quad (9.32a)$$

$$\frac{\partial H_y}{\partial t} = \frac{1}{\mu} \frac{\partial E_z}{\partial x} \quad (9.32b)$$

$$\frac{\partial E_z}{\partial t} = \frac{1}{\varepsilon} \left(\frac{\partial H_y}{\partial x} - \frac{\partial H_x}{\partial y} \right) \quad (9.32c)$$

In case of *TE* polarization, the electrical components are transverse. They are in the plane of periodicity of the PhC. On the other hand, for the *TM* polarization, the electric field is perpendicular to the directions of periodicity and the magnetic components are transverse.

Let us note that the two polarizations can be studied by the same system of equations (9.5) without separating it into two sub-systems. But to simplify the calculation codes and gain memory space, it is recommended to study these two polarizations separately.

9.2.2 Off-plane propagation

Off-plane propagation is characterized by a nonzero propagation constant k_z according to z direction. Diagram dispersion is generally determined for a fixed value of k_z . Thus, the z -derivatives in Maxwell equations become analytical while the electric and magnetic field vectors can be written as follows:

$$\vec{E}(x, y, z, t) = \vec{E}_0(x, y, t) \exp(ik_z z) \quad (9.33a)$$

$$\vec{H}(x, y, z, t) = \vec{H}_0(x, y, t) \exp(ik_z z) \quad (9.33b)$$

The Maxwell's system of equations (9.5) becomes:

$$\frac{\partial H_x}{\partial t} = \frac{1}{\mu} (ik_z E_y - \frac{\partial E_z}{\partial y}) \quad (9.34a)$$

$$\frac{\partial H_y}{\partial t} = \frac{1}{\mu} (\frac{\partial E_z}{\partial x} - ik_z E_x) \quad (9.34b)$$

$$\frac{\partial H_z}{\partial t} = \frac{1}{\mu} (\frac{\partial E_x}{\partial y} - \frac{\partial E_y}{\partial x}) \quad (9.34c)$$

$$\frac{\partial E_x}{\partial t} = \frac{1}{\varepsilon} (\frac{\partial H_z}{\partial y} - ik_z H_y) \quad (9.34d)$$

$$\frac{\partial E_y}{\partial t} = \frac{1}{\varepsilon} (ik_z H_x - \frac{\partial H_z}{\partial x}) \quad (9.34e)$$

$$\frac{\partial E_z}{\partial t} = \frac{1}{\varepsilon} (\frac{\partial H_y}{\partial x} - \frac{\partial H_x}{\partial y}) \quad (9.34f)$$

In this case, it is no longer possible to separate the system into two subsystems as before. The *TE* and *TM* cases are therefore mixed together and can not be treated separately. However, we can note that the calculation code is simplified since the z derivatives are analytically evaluated so there is no discretization along the z direction. A 2D algorithm is still needed.

9.2.3 Periodic boundary conditions

As the CPU time and space memory is limited, the FDTD calculation window must also be finite. Because of symmetry, only one unit cell is considered. To reproduce the crystal at the truncated domain boundaries, the Floquet-Bloch periodicity conditions [9] are applied to the electric and magnetic components. Despite the fact that these periodicity conditions are general and can be applied to any periodic structure, their expressions depend on the Bravais lattice. Consequently, we will consider the two most used Bravais lattices i.e. the rectangular and the triangular ones.

Rectangular cell

Let us consider a PhC made of cylinders (refractive index n_1) immersed in a medium of refractive index n_2 . a and b are the lattice constants in the x and y directions respectively (see figure 9.6). The FDTD window calculation is shown in figure 9.6-b.

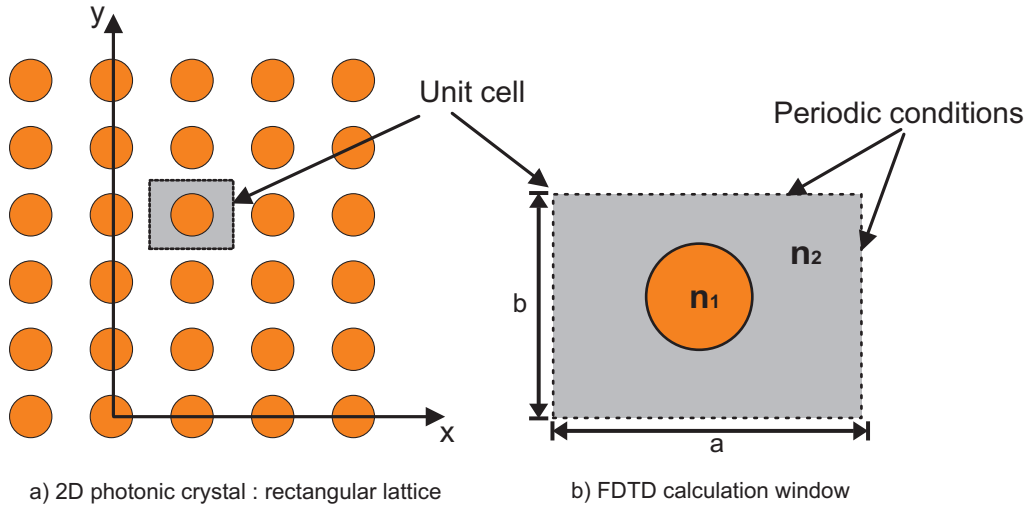


Figure 9.6: Rectangular structure and FDTD window calculation

The Floquet-Bloch conditions are applied to the electric and magnetic components as follows:

$$\vec{E}(x = 0, y, t) = \vec{E}(x = a, y, t) \exp(-ik_x \cdot a) \tag{9.35a}$$

$$\vec{E}(x, y = 0, t) = \vec{E}(x, y = b, t) \exp(-ik_y \cdot b) \tag{9.35b}$$

$$\vec{H}(x = a, y, t) = \vec{H}(x = 0, y, t) \exp(ik_x \cdot a) \tag{9.35c}$$

$$\vec{H}(x, y = b, t) = \vec{H}(x, y = 0, t) \exp(ik_y \cdot b) \tag{9.35d}$$

Triangular cell

Similarly to the rectangular cell, the calculation FDTD window is limited to a single unit cell. To model the triangular photonic structure (see figure 9.7-a), three choices of the FDTD window are possible. The first one is to take a non-orthogonal unit cell (cell 1 in figure 9.7-a) and implement the periodic boundary conditions in a Non orthogonal-FDTD algorithm [16, 17] for which the classical FDTD developed in an orthogonal coordinate system is not suitable. To bypass this constraint and remaining in the conventional FDTD with orthogonal coordinates, the second rectangular cell (celle 2 in figure 9.7-a) can be used to derive the periodic conditions. Nevertheless, this cell contains two patterns. This means that the rectangular periodic conditions lead to a less-description of all the possible solutions. Consequently, an aliasing effect will appear in the dispersion diagram.

In order to get gain in computational time and space and prevent this band folding while remaining with the orthogonal FDTD algorithm, a rectangular cell can be defined with only one pattern (cell 3 in figure 9.7-a). Within this FDTD calculation cell (9.7-b), the periodic conditions above are therefore replaced by:

-along the x direction :

$$\vec{E}(x = 0, y, z, t) = \vec{E}(x = a, y, z, t) \exp(-ik_x \cdot a) \tag{9.36a}$$

$$\vec{H}(x = a, y, z, t) = \vec{H}(x = 0, y, z, t) \exp(ik_x \cdot a) \tag{9.36b}$$

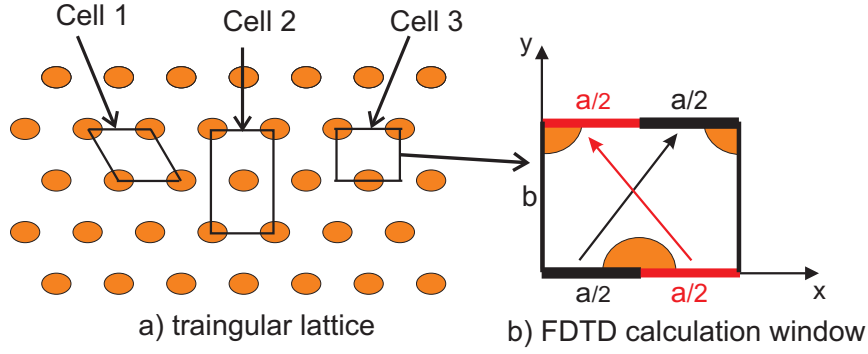


Figure 9.7: Triangular structure and FDTD calculation window

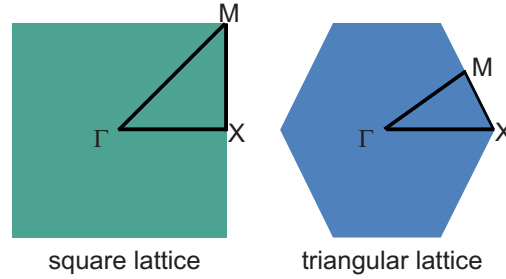


Figure 9.8: Brillouin zone

- along the y direction with $x \geq 0$ and $x \leq a/2$

$$\vec{E}(x, y = 0, z, t) = \vec{E}(x + \frac{a}{2}, y = b, z, t) \exp(i(-k_y \cdot b - k_x \cdot a/2)) \quad (9.37a)$$

$$\vec{H}(x, y = b, z, t) = \vec{H}(x + \frac{a}{2}, y = 0, z, t) \exp(i(k_y \cdot b - k_x \cdot a/2)) \quad (9.37b)$$

- along the y direction with $x > a/2$ and $x \leq a$

$$\vec{E}(x, y = 0, z, t) = \vec{E}(x - \frac{a}{2}, y = b, z, t) \exp(i(-k_y \cdot b + k_x \cdot a/2)) \quad (9.38a)$$

$$\vec{H}(x, y = b, z, t) = \vec{H}(x - \frac{a}{2}, y = 0, z, t) \exp(i(k_y \cdot b + k_x \cdot a/2)) \quad (9.38b)$$

By the way, the dispersion diagram of a triangular or honeycomb Bravais lattices can be calculated without modifying the orthogonal Cartesian Yee schema.

9.2.4 Some examples of band gap calculation

To obtain a photonic band diagram, several FDTD calculations are necessary done by varying the \vec{k} wavevector that must scan the irreducible Brillouin zone (figure 9.8). ΓX , XM and $M\Gamma$ highest symmetry directions are then discretized.

For this band gap calculation, the N-Order FDTD algorithm is used [18, 19]. This basis of this algorithm is quite simple: a signal is injected to excite all possible frequencies of the structure. This signal is introduced in accordance to the Maxwell-Gauss law ($div(\vec{E}) = 0$) and given as follows:

$$\vec{E} = \sum_{\vec{G}} (\vec{v} \wedge (\vec{k} + \vec{G})) \exp(i(\vec{k} + \vec{G}) \cdot \vec{r}) \quad (9.39)$$

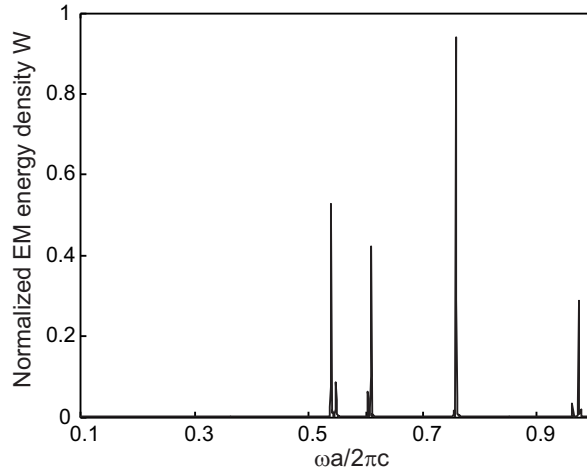


Figure 9.9: Normalized electromagnetic energy density at Γ point for triangular structure of air holes (of radius $r = 0.25a$) into lithium niobate. *TM* Polarization.

\vec{v} is a random vector, \vec{k} and \vec{G} denote the wavevector and the reciprocal lattice vector respectively.

After injecting this last initial signal, and for a given \vec{k} , the FDTD simulation is run and electromagnetic energy density time-evolution is calculated as a function of the frequency. This later is calculated through:

$$W = \frac{1}{4}(\epsilon_0 \epsilon |E|^2 + \mu |H|^2) \quad (9.40)$$

Only eigenmodes of the structure persist and evanescent ones gradually disappear. After a large number of time iterations (typically 10^5) a permanent regime is then reached and the electromagnetic energy density spectrum exhibits several peaks corresponding to the eigenfrequencies of the studied structure. An example of eigenfrequencies calculation for a triangular structure in the Γ point is shown in figure 9.9. The structure is made of air holes ($n_1 = 1$) into a dielectric medium which is lithium niobate ($LiNbO_3$) with refractive index $n_2 = 2.1421$. The radius of the holes is $r = 0.25a$ which corresponds to a filling factor of 0.2267%. The FDTD grid, one PhC period, contains 60×52 spatial grids. To satisfy the stability criterion and avoid numerical dispersion, the time step is taken as $\Delta t = a/(120 \cdot c)$.

To get the complete photonic band structure, it is necessary to scan the k values over all the contour of the irreducible Brillouin zone (ΓXM). Figure 9.10 shows the photonic band diagram calculated for both *TE* and *TM* polarizations for a structure parameters similar to those used above in the case of figure 9.9.

We can note the emergence of a photonic bandgap for $\omega a/2\pi c$ between 0.32 and 0.35 in the case of the *TE* polarization (figure 9.10-a). This band does not exist in the case of the *TM* polarization (figure 9.10-b) so it is called "partial".

Note here that, for a dispersive material, the calculation of the electromagnetic energy density is no more given by equation 9.40 that is only valid for dielectrics (no dispersion). In the case of metallic dispersive material, the electromagnetic energy density is given by (no magnetic dispersion):

$$W = \frac{1}{4} \left(\frac{\partial(\omega \epsilon_0 \epsilon)}{\partial \omega} |E|^2 + \mu |H|^2 \right) \quad (9.41)$$

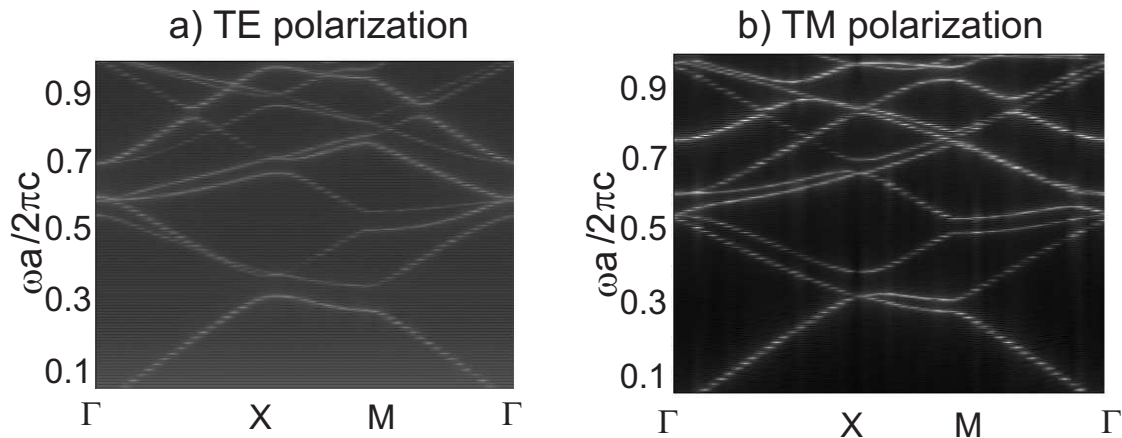


Figure 9.10: Photonic band diagram for triangular structure of air holes (of radius $r = 0.25a$) into lithium niobate.

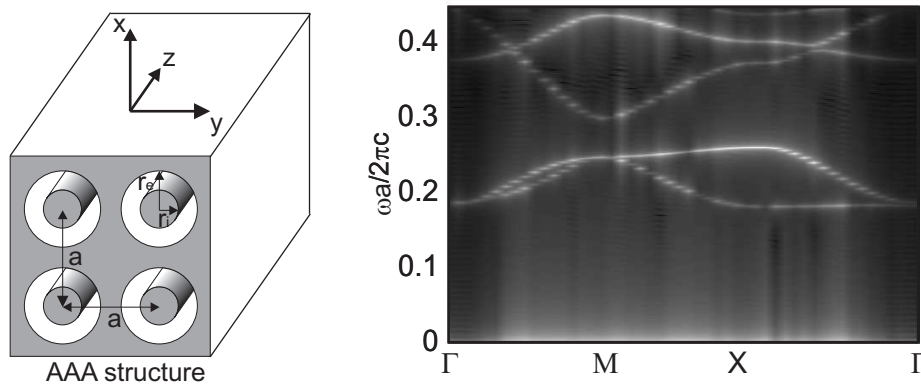


Figure 9.11: In-plane photonic band diagram for annular aperture arrays engraved into silver (TE polarization).

The calculation of the energy density depends then on the dispersion model introduced in the FDTD. Accordingly, an analytic expression of W is obtained through the calculation of the frequency derivative in equation 9.41. Its numerical value is then performed by the determination of the spectral responses of both the two electric and magnetic fields that are determined by the FDTD code.

Another example of band diagram, corresponding to a metallic structure made of annular aperture arrays (AAA) engraved into silver layer and arranged in a square lattice, is shown in figure 9.11. The AAA structure has been proposed by F. Baida and D. Van Labeke [20] for Enhanced Optical Transmission (EOT) applications. It was showed that transmission through AAA sub-wavelength structure could reach 90% in the visible range [21]. This EOT is due to the excitation and the propagation of a guided mode inside each aperture. The main transmission peak corresponds to the excitation of the TE_{11} mode at its cutoff wavelength [19]. This later only depends on the value of the inner and the outer radii. For $r_i = 50\text{nm}$ and $r_e = 75\text{nm}$ and a lattice constant of $a = 160\text{nm}$ one gets the band diagram of figure 9.11.

In case of the figure 9.11, corresponding to the TE polarization, we note the presence of two photonic bandgaps. the first is ranging from zero frequency (infinite wavelength) to the frequency value of $0.1835(c/a)$ ($\lambda = 872\text{nm}$). The second gap is in the visible range between 492nm and 630nm . Note that these bandgaps are "total" since the corresponding eigen

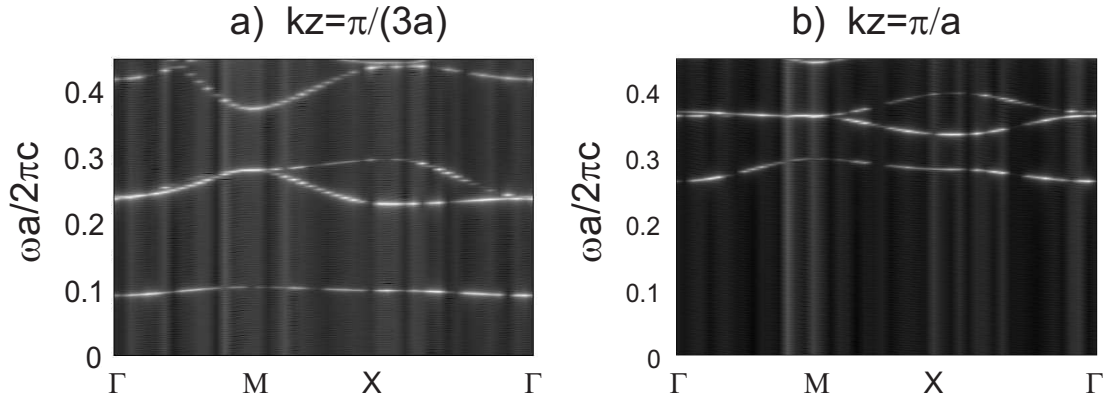


Figure 9.12: Off-plane photonic band diagram for annular aperture arrays made in silver.

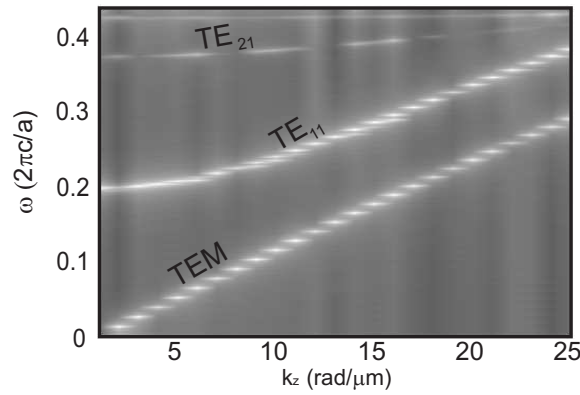


Figure 9.13: Dispersion curves at Γ point for the coaxial structure made in silver (lattice constant $a = 160$ nm, inner radius $r_i = 50$ nm and outer radius $r_e = 75$ nm; silver dispersion is modeled by a Drude model).

frequencies of *TM* polarization are located above $0.45 \times c/a$.

The figure 9.12 illustrates photonic band diagrams for the same considered AAA structure but in the case of off-plane propagation with two different values of k_z . There is occurrence of an additional photonic band relative to the in-plane case. This is due to the transverse electromagnetic (*TEM*) mode excited now at a nonzero frequency (far from the cutoff). For $k_z = \pi/(3a)$, the bandgaps are located in the ranges $]1873 \text{ nm}, \infty[$, $]723 \text{ nm}, 1668 \text{ nm}[$ and $]458 \text{ nm}, 575 \text{ nm}[$. These bandgaps become $]653 \text{ nm}, \infty[$, $]512 \text{ nm}, 574 \text{ nm}[$ and $]378 \text{ nm}, 431 \text{ nm}[$ when $k_z = \pi/a$. According to the theory, this band gap shift is due to the fact that the eigenfrequencies of guided modes increase with k_z .

Figure 9.13, showing the dispersion curves (at Γ point) of the guided modes depending on k_z , clearly confirms the *TEM* nature of the additional mode excited in the off-plan case. This mode band starts from zero frequency, and therefore has no cutoff frequency. An EOT based on the excitation of this peculiar mode can be obtained under two conditions: an oblique incidence with *TM* polarization [22]. The last section of this chapter is devoted to the study of EOT obtained through the excitation of this peculiar mode.

An example of time evolution of the electromagnetic energy density is given on figure 9.14. The considered structure is an array of coaxial waveguides made in perfectly electric conductor (PEC). All the geometrical parameters are given in the caption in addition to the FDTD simulation ones. One notes that the main peak corresponds to the TE_{21} guided mode

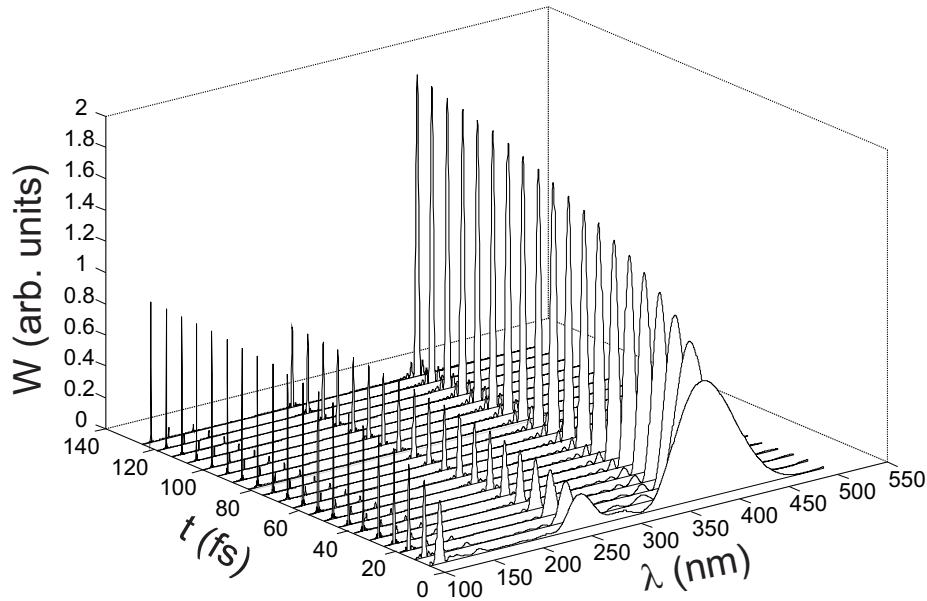


Figure 9.14: Time evolution of the electromagnetic energy density spectrum. The modeled structure is an array of coaxial waveguides made in perfectly electric conductor (PEC) and arranged in square lattice. The inner and outer radii is $r_i = 100\text{nm}$ and $r_e = 140\text{nm}$ respectively. The period of the grating is $a = 300\text{nm}$ but the obtained results are independent on this value because there is non coupling between tow adjacent waveguides. The FDTD simulations are done with a uniform spatial mesh of $\Delta x = \Delta y = \frac{a}{400}$ and the temporal step was fixed to $\Delta t = \frac{\Delta x}{4c}$ where c is the light velocity in vacuum.

that has a cutoff wavelength of $\lambda_{TE_{21}}^c = \frac{\pi(r_i+r_e)}{2}$.

9.3 Scattering calculation for 3D biperiodic nanostructures

In this section, we will focus on the FDTD modeling of dielectric and metallic bi-periodic structures. For normal incidence, the FDTD method, based on the classical Yee's scheme, is a powerful tool that can simply model such periodic structures [24, 25, 26]. In fact, in this simple case, the Floquet-Bloch periodic boundary conditions (PBC) can be easily applied without any change because these conditions are independent of the frequency. However, at oblique incidence, applying PBC implicitly involves a frequency term that must be integrated into the FDTD algorithm that operates in the temporel domain. Thus, in order to adapt FDTD to oblique incidence case, Veysoglu [27] introduced the field transformation method applied to \vec{E} and \vec{H} toward new \vec{P} and \vec{Q} fields. By the way, the PBC conditions become similar to the ones of normal incidence case nevertheless the immediate consequence of this transformation is the need to modify the Yee's scheme. Several techniques of implementation are then proposed including that of Split-Field Method (SFM) [28].

In the following, we present the reformulation of the FDTD method, based on this SFM technique to adapt it to the case of any incidence. Maxwell's equations are modified and expressed with \vec{P} and \vec{Q} variables. They are then discretized using SFM technique. To avoid reflections at the edges of the computational window, the equations in the Berenger's PML medium are also modified and expressed in the new domain within the SFM technique. In addition, the dispersion models mentioned above (Drude, Drude-Lorentz and Drude Critical point models) are also described by modifying and adapting them to the SFM technique.

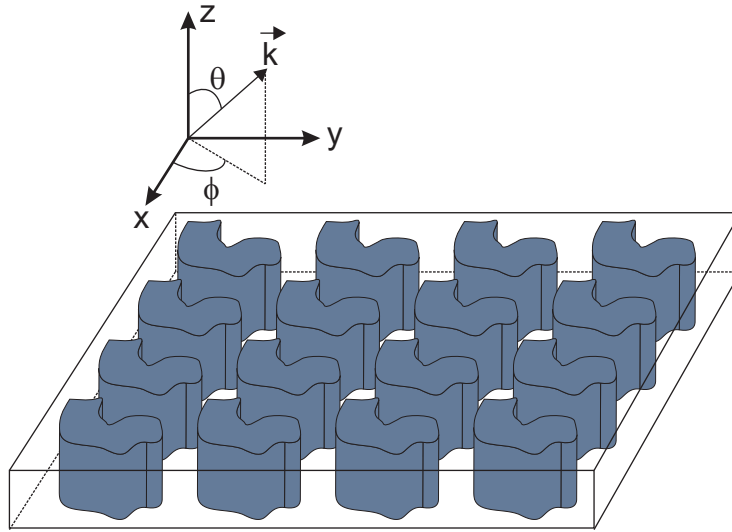


Figure 9.15: Sketch of the biperiodic structure illuminated by plane wave propagating along the \vec{k} vector defined by its Euler angles θ and ϕ .

9.3.1 Position of the problem: New $\vec{P} - \vec{Q}$ variables

Let us consider a bi-periodic structure, finished along the third direction and illuminated by a plane wave propagating at oblique incidence (see figure 9.15).

According to the notations of figure 9.15, the electric and magnetic fields of the incident plane wave can be written as:

$$\vec{E}_i = \vec{E}_{0i} e^{i[k_x \cdot x + k_y \cdot y + k_z \cdot z + \omega \cdot t]} \quad (9.42.a)$$

$$\vec{H}_i = \vec{H}_{0i} e^{i[k_x \cdot x + k_y \cdot y + k_z \cdot z + \omega \cdot t]} \quad (9.42.b)$$

where:

$$k_x = \frac{\omega}{v} \sin \theta \cos \phi \quad (9.43)$$

$$k_y = \frac{\omega}{v} \sin \theta \sin \phi \quad (9.44)$$

$$k_z = \frac{\omega}{v} \cos \theta \quad (9.45)$$

For the periodic object, a single pattern (one period) is then considered for the FDTD calculation (see figure 9.6). The periodic conditions are then written so that the fields on one side of the calculation window are expressed versus the fields on the opposite side through the Floquet-Bloch conditions. For x (lattice constant a) and y (lattice constant b) periodic structures, these conditions are expressed as follows:

$$\vec{E}(x, y, z, t) = \vec{E}(x + a, y, z, t) \cdot e^{-ik_x \cdot a} \quad (9.46.a)$$

$$\vec{E}(x, y, z, t) = \vec{E}(x, y + b, z, t) \cdot e^{-ik_y \cdot b} \quad (9.46.b)$$

$$\vec{H}(x + a, y, z, t) = \vec{H}(x, y, z, t) \cdot e^{ik_x \cdot a} \quad (9.46.c)$$

$$\vec{H}(x, y + b, z, t) = \vec{H}(x, y, z, t) \cdot e^{ik_y \cdot b} \quad (9.46.d)$$

As the FDTD method operates in the temporal domain and k_x and k_y components explicitly depend of ω , the direct application of these periodic conditions is prohibited. Consequently, a change of variables is performed so that \vec{E} and \vec{H} components are replaced by two new components \vec{P} and \vec{Q} respectively in order to eliminate the k_x and k_y dependence in the PBC. These new fields are defined as follows:

$$\vec{P} = \vec{E} \cdot e^{-ik_x x} \cdot e^{-ik_y y} \quad (9.47.a)$$

$$\vec{Q} = \vec{H} \cdot e^{-ik_x x} \cdot e^{-ik_y y} \quad (9.47.b)$$

Therefore, the new periodic conditions can be applied similarly to the case of normal incidence through the relations:

$$\vec{P}(x, y, z, t) = \vec{P}(x + a, y, z, t) \quad (9.48.a)$$

$$\vec{Q}(x + a, y, z, t) = \vec{Q}(x, y, z, t) \quad (9.48.b)$$

$$\vec{P}(x, y, z, t) = \vec{P}(x, y + b, z, t) \quad (9.48.c)$$

$$\vec{Q}(x, y + b, z, t) = \vec{Q}(x, y, z, t) \quad (9.48.d)$$

Replacing \vec{E} and \vec{H} by their expressions in terms of \vec{P} and \vec{Q} through equations 9.47 in Maxwell's equations system 9.5 leads to:

$$\frac{\partial Q_x}{\partial t} = \frac{1}{\mu_0} \left[\frac{\partial P_y}{\partial z} - \frac{\partial P_z}{\partial y} - ik_y P_z \right] \quad (9.49.a)$$

$$\frac{\partial Q_y}{\partial t} = \frac{1}{\mu_0} \left[\frac{\partial P_z}{\partial x} + ik_x P_z - \frac{\partial P_x}{\partial z} \right] \quad (9.49.b)$$

$$\frac{\partial Q_z}{\partial t} = \frac{1}{\mu_0} \left[\frac{\partial P_x}{\partial y} + ik_y P_x - \frac{\partial P_y}{\partial x} - ik_x P_y \right] \quad (9.49.c)$$

$$\frac{\partial P_x}{\partial t} = \frac{1}{\varepsilon} \left[\frac{\partial Q_z}{\partial y} + ik_y Q_z - \frac{\partial Q_y}{\partial z} \right] \quad (9.49.d)$$

$$\frac{\partial P_y}{\partial t} = \frac{1}{\varepsilon} \left[\frac{\partial Q_x}{\partial z} - \frac{\partial Q_z}{\partial x} - ik_x Q_z \right] \quad (9.49.e)$$

$$\frac{\partial P_z}{\partial t} = \frac{1}{\varepsilon} \left[\frac{\partial Q_y}{\partial x} + ik_x Q_y - \frac{\partial Q_x}{\partial y} - ik_y Q_x \right] \quad (9.49.f)$$

We can notice that for a wave propagating at normal incidence, the system (9.49) above is equivalent to the conventional Maxwell' equations expressed in $\vec{E} - \vec{H}$. Nonetheless, in the oblique case, additional terms appear in the second right members of equations (9.49) and they explicitly depend on k_x and k_y i.e. on the frequency ω . Even if these terms are equivalent to time derivatives, the direct implementation of the FDTD in this case is impossible. Many implementation techniques have been proposed [29, 30, 31, 28, 32, 33] to overcome this problem. One of them is the Split Field Method [32, 28] which will be described below.

9.3.2 Split Field Method

SFM technique is based on the split of \vec{P} and \vec{Q} field components. To illustrate the method, let us take for example the split of the Q_x component occurring in equation (9.49.a). By reducing the frequency additional term on the left hand, this equation can be written as:

$$\frac{\partial Q_x}{\partial t} + i\omega \frac{k_y}{\mu\omega} P_z = \frac{1}{\mu} \left[\frac{\partial P_y}{\partial z} - \frac{\partial P_z}{\partial y} \right] \quad (9.50a)$$

According to (9.42.a) and (9.47.a), equation (9.50a) becomes:

$$\frac{\partial}{\partial t} \left[Q_x + \frac{k_y}{\mu\omega} P_z \right] = \frac{1}{\mu} \left[\frac{\partial P_y}{\partial z} - \frac{\partial P_z}{\partial y} \right] \quad (9.51a)$$

This leads to a new component $Q_{xa} = Q_x + \frac{k_y}{\mu\omega} P_z$ which satisfies Maxwell's equation as for normal incidence. Similarly, the split of all the others components in the $\vec{P} - \vec{Q}$ domain gives:

$$Q_{xa} = Q_x + \frac{k_y}{\mu\omega} P_z \quad (9.52.a)$$

$$Q_{ya} = Q_y - \frac{k_x}{\mu\omega} P_z \quad (9.52.b)$$

$$Q_{za} = Q_z - \frac{k_y}{\mu\omega} P_x + \frac{k_x}{\mu\omega} P_y \quad (9.52.c)$$

$$P_{xa} = P_x - \frac{k_y}{\varepsilon\omega} Q_z \quad (9.52.d)$$

$$P_{ya} = P_y + \frac{k_x}{\varepsilon\omega} Q_z \quad (9.52.e)$$

$$P_{za} = P_z - \frac{k_x}{\varepsilon\omega} Q_y + \frac{k_y}{\varepsilon\omega} Q_x \quad (9.52.f)$$

The six components thereby obtained satisfy the following equations that can be discretized according to the classical Yee's scheme:

$$\frac{\partial Q_{xa}}{\partial t} = \frac{1}{\mu} \left[\frac{\partial P_y}{\partial z} - \frac{\partial P_z}{\partial y} \right] \quad (9.53.a)$$

$$\frac{\partial Q_{ya}}{\partial t} = \frac{1}{\mu} \left[\frac{\partial P_z}{\partial x} - \frac{\partial P_x}{\partial z} \right] \quad (9.53.b)$$

$$\frac{\partial Q_{za}}{\partial t} = \frac{1}{\mu} \left[\frac{\partial P_x}{\partial y} - \frac{\partial P_y}{\partial x} \right] \quad (9.53.c)$$

$$\frac{\partial P_{xa}}{\partial t} = \frac{1}{\varepsilon} \left[\frac{\partial Q_z}{\partial y} - \frac{\partial Q_y}{\partial z} \right] \quad (9.53.d)$$

$$\frac{\partial P_{ya}}{\partial t} = \frac{1}{\varepsilon} \left[\frac{\partial Q_x}{\partial z} - \frac{\partial Q_z}{\partial x} \right] \quad (9.53.e)$$

$$\frac{\partial P_{za}}{\partial t} = \frac{1}{\varepsilon} \left[\frac{\partial Q_y}{\partial x} - \frac{\partial Q_x}{\partial y} \right] \quad (9.53.f)$$

Once the updated components of \vec{P}_a and \vec{Q}_a completed, the second step of the algorithm is to calculate \vec{P} and \vec{Q} components through the system of equations (9.52) that gives after simple algebra the system below:

$$Q_z = \frac{1}{1 - \frac{k_x^2 + k_y^2}{\varepsilon\mu\omega^2}} \left[Q_{za} + \frac{k_y}{\mu\omega} P_{xa} - \frac{k_x}{\mu\omega} P_{ya} \right] \quad (9.54.a)$$

$$P_z = \frac{1}{1 - \frac{k_x^2 + k_y^2}{\varepsilon\mu\omega^2}} \left[P_{za} + \frac{k_x}{\varepsilon\omega} Q_{ya} - \frac{k_y}{\varepsilon\omega} Q_{xa} \right] \quad (9.54.b)$$

$$Q_x = Q_{xa} - \frac{k_y}{\mu\omega} P_z \quad (9.54.c)$$

$$Q_y = Q_{ya} + \frac{k_x}{\mu\omega} P_z \quad (9.54.d)$$

$$P_x = P_{xa} + \frac{k_y}{\varepsilon\omega} Q_z \quad (9.54.e)$$

$$P_y = P_{ya} - \frac{k_x}{\varepsilon\omega} Q_z \quad (9.54.f)$$

This system (9.54) needs to calculate \vec{P} and \vec{Q} components at the same time iteration as \vec{P}_a and \vec{Q}_a components. This is in contradiction with the traditional Yee's scheme. Consequently, the new (\vec{P}, \vec{Q}) and (\vec{P}_a, \vec{Q}_a) fields will be calculated at time $n\Delta t$ and time $(n + \frac{1}{2})\Delta t$ in order to reach a stable numerical schema. To this end, each component is calculated twice in one time iteration by introducing other intermediate components in the calculation program (see reference [34]).

Stability criterion

As the transition to the new $\vec{P} - \vec{Q}$ domain, the stability criterion is also modified. Based on the calculation of Kao [29, 30] and in the case of 3D uniform meshing, this later is expressed as:

$$\frac{\Delta}{\Delta t} \geq \frac{v_i}{v_i^2 \mu \varepsilon - \sin^2(\theta)} \left\{ |\sin(\theta) \cdot \cos(\varphi)| + |\sin(\theta) \cdot \sin(\varphi)| + \sqrt{3v_i^2 \mu \varepsilon - 2 \cdot \sin^2(\theta) (1 - |\sin(\varphi) \cdot \cos(\varphi)|)} \right\} \quad (9.55)$$

where v_i is the phase velocity of the incident wave and ε and μ are chosen to be the characteristics of the less dense medium in the computational domain.

Let us note here that the time step decreases with the incidence angle θ and hence the computational time becomes very long for large incidence angles. Nonetheless, the computational time is relatively acceptable up to an incidence angle of 80° .

9.3.3 Absorbing boundary conditions : PML

The implementation of absorbing boundary conditions in the oblique case requires to make a change of variables on the fields components in the PML medium similarly to the changes made in the main computational grid [34]. For x and y periodic structure, only PML is needed in the third direction (Oz). In this case, the new fields components are defined as follows:

$$P_{v\mu} = E_{v\mu} \cdot e^{-ik_x x} \cdot e^{-ik_y y} \quad (9.56.a)$$

$$Q_{v\mu} = H_{v\mu} \cdot e^{-ik_x x} \cdot e^{-ik_y y} \quad (9.56.b)$$

$$P_z = E_z \cdot e^{-ik_x x} \cdot e^{-ik_y y} \quad (9.56.c)$$

where v represents x or y and μ denotes x , y or z . $E_{v\mu}$ and $Q_{v\mu}$ are the field components in the classical PML shell corresponding to the components of the two fictitious waves resulting from the split of the plane wave inside the PML (see section 1 of this chapter). For details of implementing these PML at oblique incidence, the reader can refer to [34].

9.3.4 SFM-FDTD in dispersive media

For oblique incidence, and according to the two systems of equations (9.53) and (9.54), the components that require particular treatment in the dispersive medium are: P_{xa} , P_{ya} , P_{za} , Q_z , P_z , P_x and P_y . Direct calculation of these components by equations (9.53) and (9.54) involves the permittivity term which is frequency-dependent. In this section, we only show how to take into account the media dispersion in FDTD oblique incidence in the case of the Drude critical points model [35]. The implementation details of the other of dispersion models by SFM-FDTD are given in [36] for Debye model, and in [37] for both Drude and Drude-Lorentz models.

Let us quote that equations (9.53) for the calculation of P_{xa} , P_{ya} and P_{za} are similar to traditional Maxwell's equations. Accordingly, the calculation of these components in the dispersive medium will not require any further treatment compared to the normal incidence case. Contrarily, equations (9.54) for the Q_z , P_z , P_x and P_y need a different way to be processed.

P_{xa} , P_{ya} and P_{za} implementation: These three components are calculated in a similar way. So let us take as an example only the P_{xa} calculation. By analogy with the normal incidence case (equation 9.25), we introduced a new component L_{xa} (equivalent to the D_x component in the classical case) defined as:

$$L_{xa} = \varepsilon_0 \cdot \varepsilon_{DCP} \cdot P_{xa} \quad (9.57)$$

Equation (9.53.d) is therefore wrote as:

$$\frac{\partial L_{xa}}{\partial t} = \left[\frac{\partial Q_z}{\partial y} - \frac{\partial Q_y}{\partial z} \right] \quad (9.58)$$

The discretization of this last equation allows us to calculate the L_{xa} variable as follows:

$$L_{xa}^{n+1}(i+\frac{1}{2}, j, k) = L_{xa}^n(i+\frac{1}{2}, j, k) + \frac{\Delta t}{\Delta y} \left[Q_z^n(i+\frac{1}{2}, j+\frac{1}{2}, k) - Q_z^n(i+\frac{1}{2}, j-\frac{1}{2}, k) \right] + \frac{\Delta t}{\Delta z} \left[Q_y^n(i+\frac{1}{2}, j, k-\frac{1}{2}) - Q_y^n(i+\frac{1}{2}, j, k+\frac{1}{2}) \right] \quad (9.59)$$

Analogically to equations (9.26), (9.27.a) and (9.27.b), L_{xa} can be expressed as follows:

$$L_{xa} = L_{xaD} + \sum_{p=1}^{p=2} L_{xaCp} \quad (9.60)$$

with:

$$L_{xaD} = \varepsilon_0 \left[\varepsilon_\infty - \frac{\omega_p^2}{\omega^2 + i\gamma\omega} \right] P_{xa} \quad (9.61.a)$$

$$L_{xaCp} = \varepsilon_0 \left[A_p \Omega_p \left(\frac{e^{i\phi_p}}{\Omega_p - \omega - i\Gamma_p} + \frac{e^{-i\phi_p}}{\Omega_p + \omega + i\Gamma_p} \right) \right] P_{xa} \quad (9.61.b)$$

As before, after the inverse Fourier transforms and finite centred differences discretization of different partial derivatives, we reach the updated equations for the component P_{xa} :

$$P_{xa}^{n+1} = \frac{1}{\frac{\chi_D}{\alpha_D} + \sum_{p=1}^{p=2} \left(\frac{\chi_p}{\alpha_p} \right)} \left[L_{xa}^{n+1} + \frac{\beta_D}{\alpha_D} L_{xaD}^{n-1} + \frac{4}{\alpha_D} L_{xaD}^n - \frac{\delta_D}{\alpha_D} P_{xa}^{n-1} - \frac{4\varepsilon_0\varepsilon_\infty}{\alpha_D} P_{xa}^n + \sum_{p=1}^{p=2} \left(\frac{\beta_p}{\alpha_p} L_{xaCp}^{n-1} - \frac{4}{\alpha_p} L_{xaCp}^n \right) + \sum_{p=1}^{p=2} \left(\frac{\delta_p}{\alpha_p} \right) P_{xa}^{n-1} \right] \quad (9.62.a)$$

$$L_{xaD}^{n+1} = \frac{1}{\alpha_D} \left[-\beta_D L_{xaD}^{n-1} - 4L_{xaD}^n + \chi_D P_{xa}^{n+1} + \delta_D P_{xa}^{n-1} + 4\varepsilon_0\varepsilon_\infty P_{xa}^n \right] \quad (9.62.b)$$

$$L_{xaCp}^{n+1} = \frac{1}{\alpha_p} \left[-\beta_p L_{xaCp}^{n-1} + 4L_{xaCp}^n + \chi_p P_{xa}^{n+1} + \delta_p P_{xa}^{n-1} \right] \quad (9.62.c)$$

Q_z , P_z , P_x and P_y implementation: The calculation of the remaining components Q_z , P_z , P_x and P_y needs the introduction of other variables involving other equations. We consider as an

example the P_z component for which implementation equations are detailed. Equation (9.54.b) involves the following one:

$$\varepsilon \cdot M_z = \frac{k_x}{\omega} Q_{ya} - \frac{k_y}{\omega} Q_{xa} + \frac{k_x^2 + k_y^2}{\mu \omega^2} P_z \quad (9.63)$$

with:

$$M_z = P_z - P_{za} \quad (9.64)$$

By setting:

$$T_z = \frac{k_x}{\omega} Q_{ya} - \frac{k_y}{\omega} Q_{xa} + \frac{k_x^2 + k_y^2}{\mu \omega^2} P_z \quad (9.65)$$

equation (9.63) becomes:

$$T_z = \varepsilon \cdot M_z = \varepsilon_0 \varepsilon_{DCP} M_z \quad (9.66)$$

As considered above, the T_z component can be expressed as:

$$T_z = T_{zD} + \sum_{p=1}^{p=2} T_{zCp} \quad (9.67)$$

with:

$$T_{zD} = \varepsilon_0 \left[\varepsilon_\infty - \frac{\omega_p^2}{\omega^2 + i\gamma\omega} \right] M_z \quad (9.68.a)$$

$$T_{zCp} = \varepsilon_0 \left[A_p \Omega_p \left(\frac{e^{i\phi_p}}{\Omega_p - \omega - i\Gamma_p} + \frac{e^{-i\phi_p}}{\Omega_p + \omega + i\Gamma_p} \right) \right] M_z \quad (9.68.b)$$

Based on the inverse Fourier transforms of the equations (9.68) above, centered difference approximations for the derivatives and taking into account the equations (9.65), (9.67) and (9.66), we get:

$$M_z^{n+1} = \frac{1}{\frac{\chi_D}{\alpha_D} + \sum_{p=1}^{p=2} \left(\frac{\chi_p}{\alpha_p} \right) - \frac{k_x^2 + k_y^2}{\mu \omega^2}} \left[\frac{k_x^2 + k_y^2}{\mu \omega^2} P_z^{n+1} + \frac{k_x}{\omega} Q_{ya}^{n+1} - \frac{k_y}{\omega} Q_{xa}^{n+1} + \frac{\beta_D}{\alpha_D} T_{zD}^{n-1} + \frac{4}{\alpha_D} T_{zD}^n \right. \\ \left. - \frac{\delta_D}{\alpha_D} M_z^{n-1} - \frac{4\varepsilon_0 \varepsilon_\infty}{\alpha_D} M_z^n + \sum_{p=1}^{p=2} \left(\frac{\beta_p}{\alpha_p} T_{zCp}^{n-1} - \frac{4}{\alpha_p} T_{zCp}^n \right) + \sum_{p=1}^{p=2} \left(\frac{\delta_p}{\alpha_p} \right) M_z^{n-1} \right] \quad (9.69.a)$$

$$T_{zD}^{n+1} = \frac{1}{\alpha_D} \left[-\beta_D T_{zD}^{n-1} - 4T_{zD}^n + \chi_D M_z^{n+1} + \delta_D M_z^{n-1} + 4\varepsilon_0 \varepsilon_\infty M_z^n \right] \quad (9.69.b)$$

$$T_{zCp}^{n+1} = \frac{1}{\alpha_p} \left[-\beta_p T_{zCp}^{n-1} + 4T_{zCp}^n + \chi_p M_z^{n+1} + \delta_p M_z^{n-1} \right] \quad (9.69.c)$$

$$P_z^{n+1} = M_z^{n+1} + P_{za}^{n+1} \quad (9.69.d)$$

The equations to update the Q_z , P_x and P_y components are obtained by the same process.

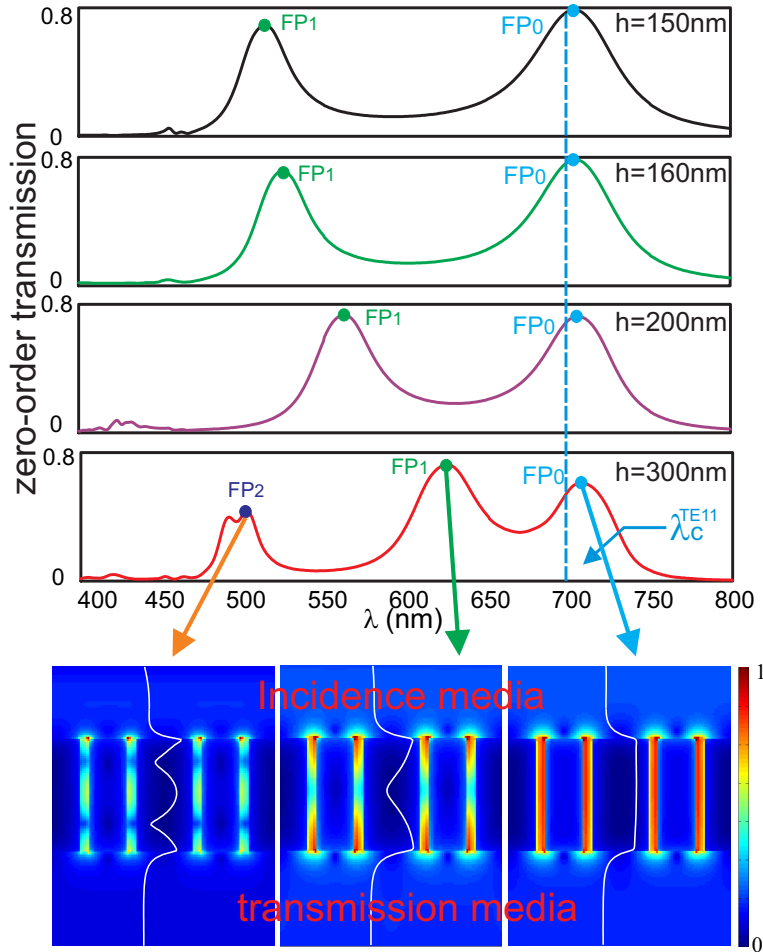


Figure 9.16: Up: Transmission spectra at normal incidence of an AAA structure made in silver film with different thicknesses values (H). The geometrical parameters of the annular apertures are $r_o = 75$ nm, $r_i = 50$ nm and the period is fixed to $a = 300$ nm. Down: Electric field intensity distributions around the apertures showing the interference patterns that take place inside them along the metal thickness direction. For FP_0 peak, the TE_{11} guided mode is excited at its cutoff wavelength so that the phase velocity tends to infinity and the effective index falls to zero. In this case, EOT occurs whatever is the value of the thickness because the phase matching condition is automatically fulfilled.

9.3.5 3D-SFM-FDTD application: EOT at oblique incidence through AAA structures

Let us recall the origin of the EOT through the AAA structure: as mentioned before, at normal incidence it is only due to the excitation of the TE_{11} guided mode inside each annular aperture. In this case, the obtained EOT is angle and polarization-independent and its spectral position corresponds to the cutoff wavelength of this guided mode. Consequently, it does not depend either on the metal thickness even if some additional peaks appear in the transmission spectrum when the thickness increases (see figure 9.16).

These peaks (named FP_m , $m \in \mathfrak{R}$ on figure 9.16) are Fabry-Perot harmonics of the TE_{11} mode that occur at fixed values of the wavelength fulfilling a phase matching condition:

$$\lambda_{TE_{11}}(m\pi - \phi_r) = 2\pi n_{eff}^{TE_{11}} H \quad (9.70)$$

where $n_{eff}^{TE_{11}}$ is the real part of the effective index of the guided mode, ϕ_r is the phase

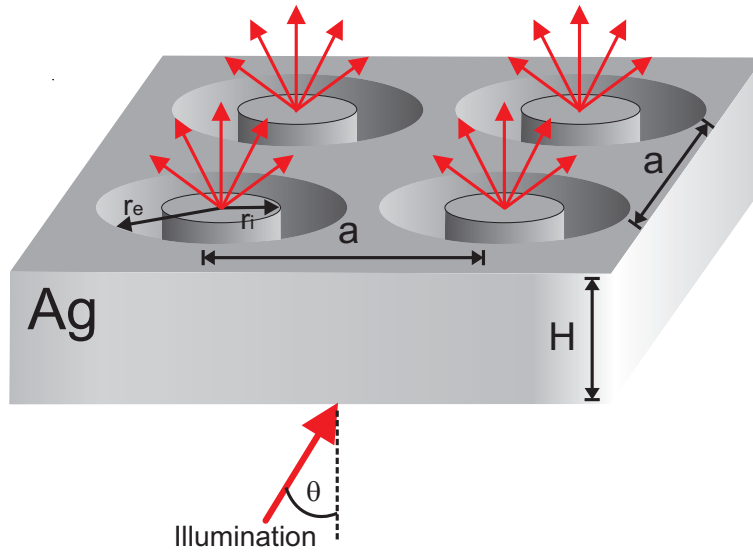


Figure 9.17: Schematic of a classical annular aperture array (AAA). r_e is the outer radius, r_i is the inner one, a is the period and θ is the angle of incidence.

change induced by the reflection on the two ends of the annular aperture and H is the metallic film thickness. At the cutoff, the effective index of the guided mode becomes very small leading to a phase matching that does not depend on the metal thickness. Nevertheless, a small spectral shift can appear between the cutoff value and the position of the transmission peak due to $\phi_r \neq 0$. This shift is clearly shown on all the spectra of figure 9.16 but it seems to be more important in the case of thicker plates (here $H = 300 \text{ nm}$). In fact, the phase ϕ_r can be seen as the result of the conversion between the incident plane wave and the guide mode through diffraction phenomenon that must depends on the metal thickness.

Let us now consider the case of oblique incidence (see figure 9.17): as mentioned before, EOT can appear through the excitation of both the TE_{11} and the TEM modes. In fact only few papers have discussed on this mode [38, 39] while its excitation conditions were recently analytically derived reference [22].

Indeed, this later is only excited with the TM polarization component of the incident beam. FDTD simulations in the case of both PEC (see figure 9.18) and real dispersive metal (figure 9 of reference [37, 40]) are done and demonstrate the occurrence of additional transmission peaks due to the excitation of the TEM guided mode. Nevertheless, others configurations such as the Slanted AAA (SAAA), that was proposed first by S. Nosal and J.J. Greffet [41], also demonstrate a possible excitation of the TEM mode for any incidence angle including normal incidence.

Moreover, as for the TE_{11} mode, the spectral position of the TEM-transmission peaks is driven by a similar phase matching condition given by equation 9.70. Nonetheless, the zero harmonic (FP_0 for $m = 0$) is now expelled to infinity and only higher orders correspond to a finite value of the wavelength. In this case, the metal thickness becomes a very important parameter that permits to adapt the transmission peak at a desired value of wavelength. Unluckily, only relatively thick metal plates allow the excitation and the propagation of the TEM mode.

Nevertheless, even if the TEM mode is excited in oblique incidence with conventional AAA (see figure 9.20a) or at normal incidence through SAAA (figure 9.20b), the transmission

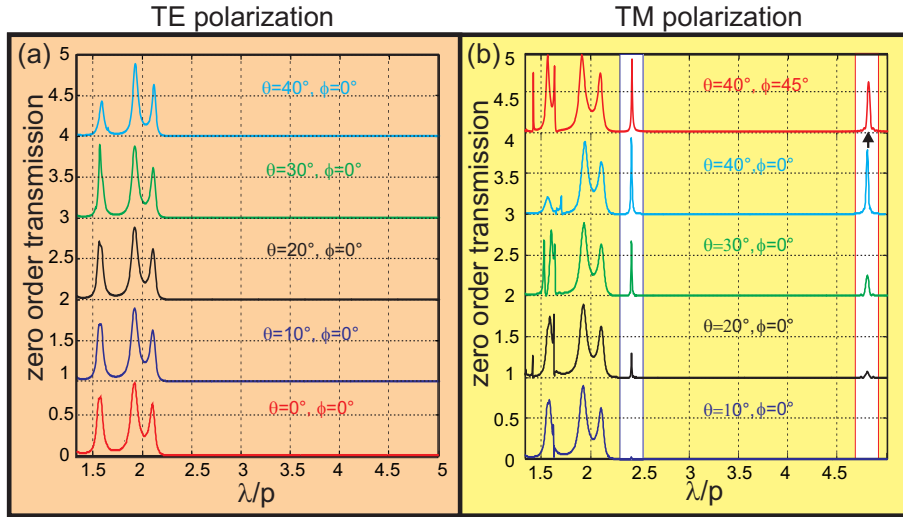


Figure 9.18: Transmission spectra through AAA structure made in perfectly electric conductor and illuminated by a TE (left) and TM (right) linearly polarized plane wave. As depicted on figure 9.15, θ and ϕ denote the incidence and azimuthal angle respectively. The geometrical parameter of the AAA structure are: $r_e = a/3, r_i = a/4$ and $H = 2a$ (please see figure 9.17 for notations). Two families of TEM peak are pointed out using two white vertical rectangles. The right one corresponds here to the first Fabry-Perot harmonic and the left one frames the second harmonic. Note that other higher harmonics also occur at smaller wavelength values.

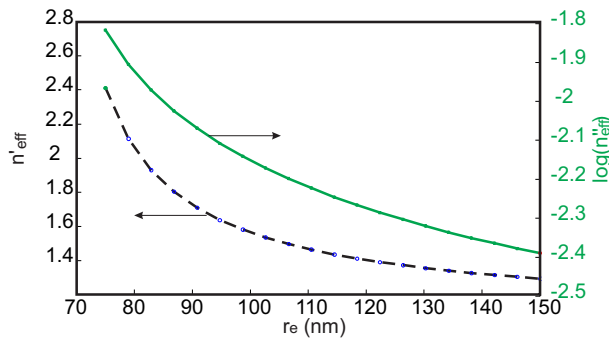


Figure 9.19: Real part n_{eff}^l and \log_{10} of the imaginary part n_{eff}^r of the effective index associated with the TEM-like mode of an infinite coaxial waveguide as a function of the outer radius r_e . The inner radius is set to $r_i = 65$ nm and the working wavelength is $\lambda = 1550$ nm.

efficiency remains very weak with regard to the TE_{11} mode. This is essentially due to metal losses. In fact, and as it can be shown in figure 9.19, the imaginary part of the effective index of the TEM-like guided mode is fairly consistent and can not be negligible.

Fortunately, another solution that is currently used in the radio-frequency domain to increase the impedance adaptation between a coaxial antenna and the vacuum can be envisaged to enhance the transmission coefficient: it consists in stretching out the central metallic part of the coaxial waveguide with respect to the outside electrode. This configuration was implicitly proposed in reference [42] to achieve 90% light transmission thanks to the excitation of the TEM mode. This kind of structure design and fabrication is readily achievable at radio frequencies. Unfortunately, this becomes more difficult in the visible range but remains possible through manufacturing process having nanometric resolution such as new generation of Focused Ion Beam.

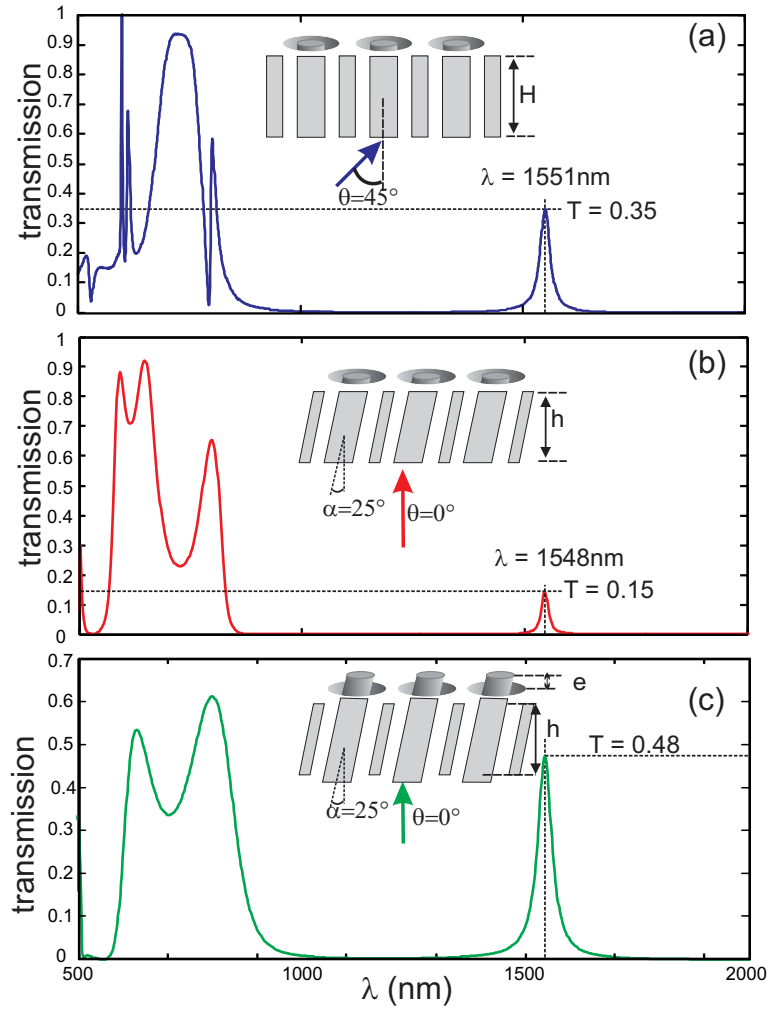


Figure 9.20: Zero-order transmission spectra for three different AAA configurations where outer and inner radii are fixed to $r_e = 130 \text{ nm}$ and $r_i = 65 \text{ nm}$ respectively. (a) Conventional structure illuminated at 45° (metal thickness of $h = 495 \text{ nm}$). (b) SAAA with tilt angle of 25° with respect to the vertical direction. The thickness of the metallic film ($h = 430 \text{ nm}$) is chosen in order to get a TEM peak transmission at $\lambda = 1550 \text{ nm}$. (c) SAAA structure with inner metallic parts that stretch out from the metallic film over a distance $e = 80 \text{ nm}$. This allows increasing of the impedance matching between the in- and out-coming plane waves with the TEM guided mode inside the apertures. The metal thickness is also adjusted in order to get a TEM peak at $\lambda = 1550 \text{ nm}$ with a transmission efficiency of 48%.

9.4 Conclusion

The FDTD is a powerful tool to model periodic and aperiodic structures. The time evolution of the electromagnetic field is directly evaluated and allows to follow the light propagation inside and around the studied structure. The SFM technique extends the FDTD capabilities to treat the diffraction problem for any incidence angle or any polarization. The integration of dispersion models such as Drude critical point allows accurate simulations that take into account the effective dispersion of noble metals in the considered spectral range especially in the visible domain. Nevertheless, the number of electromagnetic field components grows rapidly and can be larger than 100 in some particular cases (in the PML region with Drude-Lorentz dispersion model for instance). In spite of all these criticisms, the FDTD is actually one of the most used method to model experiments in Nano-Optics as attested by the number of publications in this area.

References:

- [1] K. S. Yee. Numerical solution of initial boundary value problems involving maxwell's equations in isotropic media. *IEEE Transactions on Antennas and Propagation*, 14:302–307, 1966.
- [2] A. Taflove and M. E. Brodwin. Computation of the electromagnetic fields and induced temperatures within a model of the microwave-irradiated human eye. *IEEE Transactions on Microwave Theory and Techniques*, 23:888–896, 1975.
- [3] A. Taflove and M. E. Brodwin. Numerical solution of steady-state electromagnetic scattering problems using the time-dependent maxwell's equations. *IEEE Transactions on Microwave Theory and Techniques*, 23:623–630, 1975.
- [4] K. S. Kunz and K.-M. Lee. A three-dimensional finite-difference solution of the external response of an aircraft to a complex transient em environment: Part i-the method and its implementation. *IEEE Transactions on Electromagnetic Compatibility*, 20:328–333, 1978.
- [5] R. Courant, K. O. Friedrich, and H. Lewy. On the partial difference equations of mathematical physics. *IBM Journal of Research and Development*, 11:215–234, 1967.
- [6] A. Taflove and S. C. Hagness. *Computational Electrodynamics. The Finite-Difference Time-Domain Method, 2nd ed.* Artech House, Norwood, MA, 2005.
- [7] J.-P. Berenger. A PERFECTLY MATCHED LAYER FOR THE ABSORPTION OF ELECTROMAGNETIC-WAVES. *JOURNAL OF COMPUTATIONAL PHYSICS*, 114(2):185–200, 1994.
- [8] C. F. Bohren and D. R. Huffman. *Absorption and Scattering of Light by Small Particles.* Wiley-Interscience, New York, 1983.
- [9] N. Ashcroft and N. D. Mermin. *Physique des Solides.* EDP Sciences, Les Ulis, 2002.
- [10] A. Vial, A. S. Grimault, D. Macias, D. Barchiesi, and M. Lamy de la Chapelle. Improved analytical fit of gold dispersion: application to the modeling of extinction spectra with a finite-difference time-domain method. *Phys. Rev. B*, 71:085416, 2005.
- [11] L. Novotny and B. Hecht. *Principles of Nano-optic.* Cambridge University Press, 2006.
- [12] P. G. Etchegoin, E. C. Le Ru, and M. Meyer. An analytic model for the optical properties of gold. *The Journal of Chemical Physics*, 125(16):164705, 2006.

- [13] P. Etchegoin, J. Kircher, and M. Cardona. Elasto-optical constants of si. *Phys. Rev. B*, 47:10292–10303, 1993.
- [14] F. Hao and P. Nordlander. Efficient dielectric function for fdtd simulation of the optical properties of silver and gold nanoparticles. *Chemical Physics Letters*, 446(1-3):115 – 118, 2007.
- [15] A. Vial and T. Laroche. Comparison of gold and silver dispersion laws suitable for fdtd simulations. *Applied Physics B: Lasers and Optics*, 93:139–143, 2008.
- [16] M. Qiu. *Computational methods for the analysis and design of photonic bandgap structures*. Ph. d., Royal Institute of Technology, Stockholm, 2000.
- [17] W. Kuang, W. J. Kim, and J. D. O’Brien. Finite-difference time domain method for nonorthogonal unit-cell two-dimensional photonic crystals. *J. Lightwave Technol.*, 25(9):2612–2617, 2007.
- [18] C. T. Chan, Q. L. Yu, and K. M. Ho. Order-n spectral method for electromagnetic waves. *Phys. Rev. B*, 51(23):16635–16642, 1995.
- [19] F. I. Baida, D. Van Labeke, G. Granet, A. Moreau, and A. Belkhir. Origin of the super-enhanced light transmission through a 2-d metallic annular aperture array: a study of photonic bands. *Applied Phys. B*, 79(1):1–8, 2004.
- [20] F. I. Baida and D. Van Labeke. Light transmission by subwavelength annular aperture arrays in metallic films. *Opt. Commun.*, 209:17–22, 2002.
- [21] Y. Poujet, J. Salvi, and F. I. Baida. 90% extraordinary optical transmission in the visible range through annular aperture metallic arrays. *Opt. Lett.*, 32(20):2942–2944, 2007.
- [22] F. I. Baida. Enhanced transmission through subwavelength metallic coaxial apertures by excitation of the tem mode. *Applied Phys. B*, 89(2-3):145–149, 2007. Rapid Communication.
- [23] F. I. Baida, A. Belkhir, O. Arar, E. H. Barakat, J. Dahdah, C. Chemrouk, D. Van Labeke, C. Diebold, N. Perry, and M.-P. Bernal. Enhanced optical transmission by light coaxing: Mechanism of the tem-mode excitation. *Micron*, 41:742–745, 2010.
- [24] W.-J. Tsay and D. M. Pozar. Application of the fdtd technique to periodic problems in scattering and radiation. *IEEE Microwave and Guided Wave Letters*, 3:250–252, 1993.
- [25] A. Alexanian, N. J. Koliass, R. C. Compton, and R. A. York. Three-dimensional fdtd analysis of quasi-optical arrays using floquet boundary conditions and berenger’s pml. *IEEE Microwave and Guided Wave Letters*, 6:138–140, 1996.
- [26] F. I. Baida and D. Van Labeke. Three-dimensional structures for enhanced transmission through a metallic film: Annular aperture arrays. *Phys. Rev. B*, 67:155314, 2003.
- [27] M. E. Veysoglu, R. T. Shin, and J. A. Kong. A finite-difference time-domain analysis of wave scattering from periodic surfaces: Oblique-incidence case. *J. Elect. Waves Appl.*, 7:1595–607, 1993.

- [28] J. A. Roden, S. D. Gedney, M. P. Kesler, J. G. Maloney, and P. H. Harms. Time-domain analysis of periodic structures at oblique incidence: orthogonal and nonorthogonal fdtd implementations. *IEEE Transactions on Microwave Theory and Techniques*, 46:420–427, 1998.
- [29] Y.-C. A. Kao and R. G. Atkins. A finite difference-time domain approach for frequency selective surfaces at oblique incidence. *IEEE Antennas and Propagation Society International Symposium*, 2:1432–1435, 1996.
- [30] Y.-C. A. Kao. *Finite-difference time domain modeling of oblique incidence scattering from periodic surfaces*. Master's thesis, Massachusetts Institute of Technology, 1997.
- [31] J. A. Roden. *Electromagnetic analysis of complex structures using the fdtd technique in general curvilinear coordinates*. Ph.d. thesis, University of Kentucky, Lexington, KY, 1997.
- [32] P. H. Harms, J. A. Roden, J. G. Maloney, and M. P. Kesler. Numerical analysis of periodic structures using the split-field algorithm. In *13th Annual Review of Progress in Applied Computational Electromagnetics*, pages 104–111, 1997.
- [33] A. Aminian and Y. Rahmat-Samii. Spectral fdtd: a novel technique for the analysis of oblique incident plane wave on periodic structures. *IEEE Transactions on Antennas and Propagation*, 54:1818–1825, 2006.
- [34] A. Belkhir and F. I. Baida. Three-dimensional finite-difference time-domain algorithm for oblique incidence with adaptation of perfectly matched layers and nonuniform meshing: Application to the study of a radar dome. *Phys. Rev. E*, 77(5):056701, 2008.
- [35] M. Hamidi, F. I. Baida, A. Belkhir, and O. Lamrous. Implementation of the critical points model in a sfm-fdtd code working in oblique incidence. *J. Phys. D: Appl. Phys.*, 44(24):245101, 2011.
- [36] F. I. Baida and A. Belkhir. Split-field fdtd method for oblique incidence study of periodic dispersive metallic structures. *Opt. Lett.*, 34(16):2453–2455, 2009.
- [37] A. Belkhir, O. Arar, S. S. Benabbes, O. Lamrous, and F. I. Baida. Implementation of dispersion models in the split-field–finite-difference-time-domain algorithm for the study of metallic periodic structures at oblique incidence. *Phys. Rev. E*, 81(4):046705, 2010.
- [38] J. Rybczynski, K. Kempa, A. Herczynski, Y. Wang, M. J. Naughton, Z. F. Ren, Z. P. Huang, D. Cai, and M. Giersig. Subwavelength waveguide for visible light. *Appl. Phys. Lett.*, 90:021104, 2007.
- [39] T. Thio. Photonic devices: Coaxing light into small spaces. *Nature Nanotechnology*, 2:136–138, 2007.
- [40] D. Van Labeke, D. Gérard, B. Guizal, F. I. Baida and L. Li. An angle-independent Frequency Selective Surface in the optical range *Opt. Express*, 14, 11945–11951, 2006.
- [41] Samuel Nosal. *Modélisation de structures périodiques et matériaux artificiels. Application à la conception d'un radôme passe-bande*. PhD thesis, Ecole Centrale Paris, 2009.

- [42] K. Kempa, X. Wang, Z. F. Ren, and M. J. Naughton. Discretely guided electromagnetic effective medium. *Appl. Phys. Lett.*, 92:043114, 2008.